Aubineau, Jérémie, Albani, Abderrazak El, Chi Fru, Ernest , Kipp, Michael A., Ikouanga, Julie Ngwalghoubou and Bekker, Andrey 2021. Benthic redox conditions and nutrient dynamics in the ca. 2.1 Ga Franceville sub-basin. Precambrian Research 360 , 106234. 10.1016/j.precamres.2021.106234

Publishers page: http://dx.doi.org/10.1016/j.precamres.2021.106234

Benthic redox conditions and nutrient dynamics in the *ca*. 2.1 Ga Franceville sub-basin

Jérémie Aubineau[1,2*], Abderrazak El Albani[1], Ernest Chi Fru[3], Michael A. Kipp[4,5,6], Julie Ngwalghoubou Ikouanga[1] & Andrey Bekker[7,8]

[1]UMR 7285 CNRS IC2MP, University of Poitiers, Poitiers, France

[2]Géosciences Montpellier, UMR 5243, CC 60 – University of Montpellier, Montpellier, France

[3]Centre of Geobiology and Geochemistry, School of Earth and Ocean Sciences, College of Physical Sciences and Engineering, Cardiff University, Cardiff CF10 3AT, Wales, UK

[4]Department of Earth & Space Sciences and Astrobiology Program, University of Washington, Seattle, WA, 98115, USA

[5]Virtual Planetary Laboratory, NASA Nexus for Exoplanet System Science, Seattle, WA, 98115, USA

[6]Division of Geological and Planetary Sciences, California Institute of Technology, Pasadena, CA 91125, USA

[7]Department of Earth and Planetary Sciences, University of California, Riverside, CA, 92521, USA

[8]Department of Geology, University of Johannesburg, Auckland Park 2006, South Africa

*corresponding author: jeremie.aubineau@univ-poitiers.fr

Abstract

The co-existence of motile macroorganisms and mat-building cyanobacteria in the Paleoproterozoic FB_2 Member of the Franceville sub-basin, Gabon, points to the possible emergence of multi-trophic-level biological interaction by 2.1 billion years (Ga) ago. However, it is uncertain how these shallow-marine communities acquired and cycled nitrogen, a key, biolimiting nutrient required to sustain life at all trophic levels. Here, we use carbon and nitrogen isotope data from ancient microbial mats and host sediments, in combination with bottom-water redox proxies, to constrain biogeochemical processes operating in these settings. In this shallow-marine upwelling zone, iron speciation data and redox-sensitive metal concentrations point to oxygen-deficient bottom waters, which were episodically renewed with upwelling deep anoxic waters rich in nutrients and manganese. Organic carbon and nitrogen isotopes show little difference between the mat-related structures (MRS) and host sediments, suggesting either that similar metabolisms operated in benthic and planktonic microbial communities or that benthic carbon fixation contributed organic matter to the host sediments. The isotopic fractionation between organic and inorganic carbon is as large as 44‰, implying the involvement of multiple levels of heterotrophic carbon processing, linked to phototrophy, secondary productivity, and methanotrophy. Whole-rock nitrogen isotope values in the range of -3.5 to +1.9‰ are consistent with microbial community nitrogen fixation in a nitrate-limited ecosystem. These data suggest that nitrogen fixation, common in photosynthetic microbial mats in modern environments, operated in benthic settings in the coastal area of the mid-Paleoproterozoic Franceville sub-basin. The upwelling of deep, anoxic waters invoked for deposition of the upper part of the underlying FB_1 Member suggests that basin-scale redox structure modulated nitrate availability in this otherwise oxic, shallow-marine basin shelf environment.

Keywords

Mat-related structures, Paleoproterozoic, nitrogen isotopes, paleoredox, basinal structure, Francevillian biota

Introduction

The Paleoproterozoic Era, 2.5–1.6 billion years ago (Ga), was a time of profound change in atmosphere-ocean chemistry, including the so-called “Great Oxidation Event” (GOE; Holland, 2002; Bekker *et al.*, 2004) that promoted the global emergence of oxidizing conditions at Earth’s surface over an interval of 300 million years (Bekker and Holland, 2012; Lyons et al., 2014). The onset of the GOE, constrained by the disappearance of mass-independent fractionation in sulfur isotopes at *ca.* 2.46-2.43 Ga (Gumsley et al., 2017; Warke et al., 2020), records a rise in atmospheric oxygen above 10^{-5} times present atmospheric level (Farquhar et al., 2001; Pavlov and Kasting, 2002). Evidence for oxygenated surface environments comes from sedimentary and geochemical proxies including the disappearance of redox-sensitive detrital minerals, the appearance of red beds and sulfate evaporites, and enrichment of redox-sensitive trace elements in iron formations and organic-rich shales (Bankole et al., 2016; Bekker et al., 2006; Chi Fru et al., 2019, 2016; Kipp et al., 2017; Konhauser et al., 2011; Melezhik et al., 2005; Partin et al., 2013; Rasmussen and Buick, 1999; Schröder et al., 2008; Scott et al., 2008).

The redox-sensitivity of the biogeochemical cycle of nitrogen (N) - an essential nutrient needed for the construction of biomolecules in all known living organisms - has resulted in dramatic redox transformation of the N cycle as the redox state of the Earth’s surface evolved through time (Stüeken et al., 2016). The primary source of nitrogen to the biosphere is assimilation of dinitrogen (N_2) into biomass by nitrogen-fixing organisms (diazotrophs). In oxygen-depleted settings, biologically mediated degradation of diazotrophic biomass produces bioavailable ammonium (NH_4^+). In oxygen-rich waters, NH_4^+ is rapidly oxidized to nitrite (NO_2^-) and nitrate (NO_3^-) via the stepwise process of bacterial nitrification. These bioavailable N forms can be assimilated directly or returned to the atmosphere as N_2 via denitrification (*i.e.*, reduction of NO_3^- to N_2) and anaerobic ammonium oxidation (anammox; NH_4^+ oxidation coupled to NO_2^- reduction). These microbial N removal pathways are prevalent in modern oxygen-minimum zones (Dalsgaard et al., 2005; Sigman et al., 2009), meaning that oxygen-deficient waters are likely to become depleted in dissolved N. Thus, studying the response of the N cycle to Earth’s oxygenation can not only yield more precise constraints on water column redox conditions, but also can be informative about N availability for early marine ecosystems.

Because the stable isotopes of N are fractionated during the redox transformations mentioned above, many studies leverage N isotope ratios in ancient marine sedimentary rocks as a means to study the N cycle in deep time (reviewed in Ader *et al.*, 2016). This includes recent studies that have used N isotopes to infer that aerobic N cycling emerged in a stepwise fashion during the GOE (Cheng et al., 2019; Kump et al., 2011; Luo et al., 2018; Zerkle et al., 2017) and was pervasive in the surface oceans during much of the Paleoproterozoic (Kipp et al., 2018). These studies focused on the global-scale evolution of the marine N cycle across the GOE; however, the basin-scale impact of redox fluctuations, linked to extant N fixing and assimilating communities, as well as episodic incursions of anoxic deep waters, has not yet been studied for the late stage or the immediate aftermath of the GOE. Here, we explore N redox dynamics in the middle Paleoproterozoic Franceville sub-basin of Gabon with a particular focus on a sedimentary interval that bears large macrofossils and microbial mat-related structures (MRS). This allowed us to explore the relationships among redox structure, nutrient cycling, and the early evolution of complex life in this pivotal interval.

The timing of deposition in the Franceville sub-basin corresponds in age to the end of the Lomagundi Event (LE) (~2.22–2.06 Ga; Karhu & Holland, 1996; Canfield *et al.*, 2013). This event represents the longest-lived positive carbon isotope excursion in Earth's history, during which atmospheric oxygen levels rose considerably (Bekker and Holland, 2012; Planavsky et al., 2012). The *ca*. 2.1 Ga Franceville sub-basin records frequent eustatic changes and episodic upwelling of deep, anoxic waters into shallow-marine, oxic settings (Gauthier-Lafaye and Weber, 2003; Ossa Ossa et al., 2018; Reynaud et al., 2017) that could have influenced the spatiotemporal dynamics of the N cycle. As only one stratigraphic unit of the Francevillian Group (FC_1 Member) has been the focus of N isotope study so far (Kipp et al., 2018), there remains a considerable gap in our understanding of N cycling throughout the whole Francevillian Group sedimentary record. Furthermore, the Francevillian Group sedimentary rocks have revealed tantalizing evidence that the earliest potential multicellular life (El Albani et al., 2014, 2010) capable of locomotion (El Albani et al., 2019) flourished next to benthic microbial mats (Aubineau et al., 2018; El Albani et al., 2019; Reynaud et al., 2017). The microbial features, preserved as MRS, display a wide range of surface morphologies with mat-growth and mat-protected patterns. The former, including "elephant-skin" textures (EST), domal buildups, and discoidal microbial colonies, consist of the mat layer itself generated through mat propagation, while the latter, such as wrinkle and "*Kinneyia*" structures, arose from structures that relied on the mat communities for their preservation/protection. Individual MRS vary between 0.2 and 3 mm in thickness; this heterogeneity has been attributed to changes in physical and chemical environmental factors (Aubineau et al., 2020). According to their sulfur content (0.15 to 29.37 wt. %), the Francevillian MRS are further divided into unpyritized EST (0.15 to 0.36 wt. %), poorly pyritized MRS (0.19 to 4.16 wt. %), and pyritized MRS (6.46 to 29.37 wt. %) (cf. Aubineau et al., 2020). Detailed descriptions of textural diversity and elemental geochemistry of MRS are provided in Aubineau et al. (2020, 2018).

Morphological and microtextural observations have shown that the MRS were likely dominated by cyanobacterial communities (Aubineau et al., 2019, 2018). In modern environments, similar microbial mat communities are capable of “fixing” atmospheric nitrogen into bioavailable nitrogen that is subsequently utilized by microorganisms (Bebout et al., 1994; Herbert, 1999). Nitrogen fixation fulfills the N requirement for primary production, thus sustaining mat growth. Cyanobacterial mats exhibit high annual N fixation activity in the range of 0.8 to 76 g N m^{-2} $year^{-1}$, fueling high rates of CO_2 reduction during photosynthesis (Herbert, 1999; Woebken et al., 2015). This bioavailable nitrogen produced by diazotrophs is entirely consumed by the wide array of microorganisms existing within the mat (Bebout et al., 1994). Hence, the Francevillian Group mats could show a similar pattern of N cycling as there is no *a priori* reason to believe that Precambrian mats behaved differently from their modern counterparts.

In order to provide further insight into N cycling and microbial biogeochemistry at the end of the LE, this study focused on the MRS and their associated host sediments of the Francevillian Group FB_2 Member. Both have been previously characterized for their mineralogy and elemental composition (Aubineau et al., 2020, 2019). Here, we use iron-based redox analyses and redox-sensitive element concentrations to constrain local redox conditions in the depositional setting. We additionally measured organic carbon ($\delta^{13}C_{org}$) and whole-rock plus kerogen-bound nitrogen ($\delta^{15}N$) isotope compositions of both the microbial structures and host rocks to highlight potential differences related to microbial ecology (*i.e.*, benthic *vs.* planktonic communities) among the diverse lithologies. In conjunction with previously published data (Kipp et al., 2018; Ossa Ossa et al., 2018), we explore the spatial and temporal trends in C and N isotope records of the Upper Francevillian Group to constrain the basin-scale trajectory of C and N cycling at the end of the LE, and implications for the unique macrofossil record of the Franceville sub-basin.

Geological setting

The Francevillian Group in southeastern Gabon comprises five sedimentary formations (FA to FE) deposited during the middle Paleoproterozoic (Fig. 1a). This 1.0 to 2.5 km-thick sedimentary succession rests unconformably on the Archean crystalline basement (Fig. 1b; Weber, 1968). The basal FA Formation, consisting mainly of fluvial to fluvio-deltaic sandstones accumulated during a progressive basin opening to marine conditions (Bankole et al., 2015; Gauthier-Lafaye and Weber, 1989), is widely known for post-depositional uranium ore deposits hosted in the Upper FA Formation (Bankole et al., 2016; Gauthier-Lafaye and Weber, 2003, 1989). After a period of tectonic subsidence and deepening in the foreland basin (cf. Bankole et al., 2018; Ossa Ossa et al., 2020), the FA formation gave way to a predominantly marine depositional phase, starting with the FB Formation. The latter is lithostratigraphically subdivided into FB_1 (including a, b, and c units) and FB_2 (a and b units) members (Azziley Azzibrouck, 1986; Weber, 1968).

The FB_{1a} unit consists entirely of green shales, while the FB_{1b} unit contains both black shales and heterolithic beds, with the latter characterized by rhythmic couplets of greyish shale and dolomite-cemented siltstones (Reynaud et al., 2017). Following an episode of sea level rise, deposition continued with the FB_{1c} unit characterized by black shales, the upper part of which contains iron- and manganese-rich sediments (Gauthier-Lafaye and Weber, 2003). Episodic submarine volcanism and hydrothermal activity have been inferred as the potential sources of aqueous Fe(II) and Mn(II), transported from deep anoxic settings onto the basin margin by upwelling to form the Fe and Mn deposits (Ossa Ossa et al., 2018). These upwelling events brought reductants and nutrients onto the oxic, shallow-marine basin shelf (Gauthier-Lafaye and Weber, 2003), which would have driven oxygen consumption, contributing to the first of two steps in seawater deoxygenation in the Franceville sub-basin at the end of the LE (Ossa Ossa et al., 2018).

The FB_{2a} unit, formed during sea level fall (Reynaud et al., 2017), is characterized by massive sandstones with black shale interbeds and overlain by laminated black shales of the FB_{2b} unit, frequently intercalated with cm-thick siltstone layers. The FB_2 Member was deposited in a mud-dominated setting with high-density sand flows (Reynaud et al., 2017). The multiple sulfur isotope composition of authigenic pyrite in these units indicates that the seawater column during their deposition was relatively oxygenated with a sizable sulfate reservoir (Canfield et al., 2013; El Albani et al., 2019; Ossa Ossa et al., 2018). In addition, the black shales of the FB_{2b} unit host well-preserved complex macrofossils and delicate MRS (Aubineau et al., 2018; El Albani et al., 2019, 2014, 2010).

The overlying FC Formation, deposited mainly in a tidal-flat setting, is further divided into the FC_1 and FC_2 members based on lithological composition (Ossa Ossa et al., 2018). The Lower FC Formation consists of massive dolostones and black shales (Préat et al., 2011; Weber, 1968) with manganese-rich sediments at the top (Ossa Ossa et al., 2018), while the Upper FC Formation is dominated by stromatolitic chert associated with the oldest Gunflint-type assemblage of microfossils that includes filamentous cyanobacteria (Bertrand-Sarfati and Potin, 1994; Lekele Baghekema et al., 2017). The FD Formation contains marine fine- to medium-grained sedimentary rocks alternating with volcanic tuffs (Thiéblemont et al., 2014), above which the sandstones of the FE Formation were deposited (Gauthier-Lafaye and Weber, 1989; Thiéblemont et al., 2014).

Although the depositional age is still controversial and poorly resolved (Fig. 1b) (e.g., Bros et al., 1992), precise U-Pb zircon ages of 2083 ± 6 Ma and 2072 ± 29 Ma were reported from ignimbrite tuffs and sandstones near the top of the FD Formation, respectively (Horie et al., 2005; Thiéblemont et al., 2009). Based on the falling limb of the large-magnitude positive excursion in $\delta^{13}C$ recorded in marine carbonates ($\delta^{13}C_{carb}$) of the FB and lower FC formations, these units are thought to have been deposited at the end of the LE (Canfield et al., 2013; El Albani et al., 2010; Ossa Ossa et al., 2018; Préat et al., 2011). The similar end to the positive $\delta^{13}C_{carb}$ excursion observed in the lowermost part of the *ca.* 2.0 Ga Zaonega Formation (ZF; Karelia Craton, NW Russia; Hannah et al., 2008; Martin et al., 2015), together with similar large negative excursions large in $\delta^{13}C_{org}$ values below 40‰ in both the FD Formation and ZF, have led to the interpretation that these formations might have been deposited contemporaneously (Canfield et al., 2013; Kump et al., 2011). Therefore, deposition of both the FD Formation and ZF most likely corresponds to the aftermath of the LE.

A different view was recently presented by (Mayika et al., 2020), who argued that carbon isotope composition of marine carbonates in the Franceville sub-basin reflects basinal stratification with waters in shallow-marine settings having highly positive C isotope values, while waters in deep-marine settings having near-to-zero C isotope values with the difference approaching 10‰. Mayika *et al.* (2020) related highly positive C isotope values in shallow-water carbonates in the Franceville sub-basin to either high degree of evaporation or high primary productivity in these settings. In other words, this study speculated that the carbon cycle variations in the Franceville sub-basin reflect only regional, basin-scale conditions. However, this extreme level of C-isotope fractionation between shallow and deep waters and deposits is not observed in modern or ancient open-marine settings nor predicted on the theoretical grounds for the Paleoproterozoic $p\mathrm{CO}_2$ (Bjerrum and Canfield, 2004; Hotinski et al., 2004; Kroopnick, 1985, 1974). In contrast, modern, stratified basins with restricted communication with the ocean (*e.g.*, Black Sea and Kyllaren Fjord) develop similar gradients, but with highly negative C isotope values in deep waters, rather than highly positive C isotope values in shallow-water settings (Fry et al., 1991; Smittenberg et al., 2004). Mayika *et al.* (2020) related highly positive C isotope values in shallow-water carbonates in the Franceville sub-basin to either high degree of evaporation or high primary productivity in these settings. The FC Member also does not show extensive development of evaporites (Bouton et al., 2009a) nor does it show any evidence for enhanced productivity (such as a signal of nitrogen fixation;

e.g., Kipp *et al.* (2018). In contrast, mid-Proterozoic carbonate successions with a strong evaporite signal or a signal for enhanced primary productivity do not show high ^{13}C-enrichments (Kah et al., 2001; Papineau et al., 2009). Furthermore, in the case of the Mayika *et al.* (2020) study, carbon isotope values started to decrease ~10 meters below the transgressive surface, which is inconsistent with the proposed basinal stratification and agrees with a global, secular control. We thus favor the view that the FC Formation records the end of the LE at *ca.* 2.11-2.06 Ga (see Bekker et al. (2021) for further discussion of Mayika et al. (2020)).

Methods

Sampling. All of our samples (both MRS and host sediments) came from outcrops in the Moulendé Quarry (Fig. 1a). Before collecting outcrop material, the weathered outermost surfaces were removed. We carefully separated the mat laminae from its host rock material with a stainless steel razor blade – avoiding as much as possible contamination – for geochemical analyses. The host sediments were sampled directly below the MRS with a hammer. We made a special effort to exclude contribution of MRS to the host rocks during sample preparation. We cannot entirely rule out small contribution of the underlying sediment to sampled MRS, however, our sampling procedure did not result in significant contamination as far as distinct clay minerals and geochemical compositions were observed for samples of the MRS and their host sediments (Aubineau et al., 2020, 2019).

Scanning electron microscopy. Pyrite morphology of MRS and black shales was studied in carbon-coated and polished slab sections, using a FEI Quanta 200 scanning electron microscope (SEM) equipped with an energy-dispersive X-Ray Spectrometer (EDX) at the University of Lille. The images of pyrite texture were acquired in back-scattered electron (BSE) mode operated at accelerating voltage of 15 kV, 1 nA beam current, and a working distance of 10.5 mm. Pyrite was specifically targeted for textural analysis to evaluate its morphology and preservation, as it can be readily affected by oxidative weathering.

Whole-rock analysis. Major and trace element concentrations in powdered samples were analyzed by inductively coupled plasma optical emission spectrometry (ICP-OES) and inductively coupled plasma mass spectrometry (ICP-MS) at *Service d'Analyse des Roches et Minéraux* (SARM) of the *Centre de Recherches Pétrographiques et Géochimiques* (CRPG), Nancy, France. The extended protocol for major and trace element measurements at SARM-CRPG is described by Carignan *et al.* (2001). Specifically, powdered samples were decomposed using alkali fusion. They were fused with 900 mg of ultra-pure lithium metaborate at 980°C to form a glass. Then, the glass was dissolved in a mixture of 1 M nitric acid, 0.5% hydrogen peroxide, and 10% glycerol. The uncertainty for major elements was determined to be better than 5%, with the exception of Ca (10%) and P (>25%), while that for trace elements was lower than 5% for concentrations >10 ppm and 15% for concentrations between 10 and 1 ppm and >25% for elemental concentrations near the detection limit, as checked with international standards and analysis of replicate samples (cf. Carignan *et al.*, 2001).

Enrichment factors (EF) were calculated for Mn, P, Co, Cu, Mo, Ni, U, and V following the approach described by Tribovillard *et al.* (2006). EF represents the trace metal (TM) excess in the sediments, which is assessed by dividing TM/Al or TM/Ti ratios by that for the upper crustal average (Rudnick and Gao, 2003). We present in Table S1 ratios of P/Ti and P/Al as detrital tracers for P, following previous studies (*e.g.*, Filippelli et al., 2007, 2003; Latimer and Filippelli, 2001; Tribovillard et al., 2006)

Iron speciation analysis. Iron speciation analysis was performed at Cardiff University, according to the method of Poulton and Canfield (2005), which is reviewed elsewhere (Poulton and Canfield, 2011; Raiswell et al., 2018). This method targets iron that is "highly reactive" (Fe_{HR}) towards hydrogen sulfide in the form of (oxyhydr)oxides (Fe_{Mag} and Fe_{Ox}), carbonates (Fe_{carb}), and pyrite iron (Fe_{py}) relative to total iron (Fe_T), including poorly reactive Fe (Fe_{PRS}) and unreactive Fe (Fe_U). First, Fe_{Carb} was extracted with a sodium acetate buffer at pH 4.5 and 50°C for 48 hours, followed by Fe_{Ox} extraction using sodium dithionite at pH 4.8 and room temperature for 2 hours, and finally Fe_{Mag} extraction using ammonium oxalate at pH 3.2 and room temperature for 6 hours. Fe_{PRS} was then determined by boiling in 12 M HCl for 2 minutes. Fe_{Py} was measured by weighing a CuS precipitate after HCl and chromous chloride distillation, with Fe calculated assuming FeS_2 stoichiometry (Canfield et al., 1986). Replicate analyses between runs (n = 5) gave an average standard deviation of 0.11 wt.% for Fe_{Carb}, 0.19 wt.% for Fe_{Ox}, 0.004 wt.% for Fe_{Mag}, 0.07 wt.% for Fe_{PRS}, and 0.06 wt.% for Fe_{Py}. Samples containing <0.5 wt.% Fe were excluded from the iron speciation analysis. This threshold is recommended to avoid samples that are at the resolution limit of the iron-based redox proxy (see Clarkson *et al.*, 2014; Raiswell *et al.*, 2018 for reviews).

Kerogen extraction. Kerogen was isolated from selected whole-rock powders (n = 10) at the University of Washington using the published protocol from Kipp *et al.* (2018). In brief, sample powders were treated with a 1:1 mixture of concentrated HF and DI-H_2O in order to dissolve silicate minerals. The resulting solutions were centrifuged and the supernatant was decanted. Residual fluoride minerals were then dissolved with a BF_3 solution, and the supernatant decanted after centrifugation. The remaining kerogen was then rinsed with three iterations of DI-H_2O, and finally placed into a freeze-drier to remove all moisture prior to analysis.

Carbon and nitrogen isotope analyses. Carbon isotope ratios for organic matter ($\delta^{13}C_{org}$) and whole-rock N isotope values ($\delta^{15}N_{WR}$) were analyzed for all lithologies (n = 34). The isotope data were measured by flash combustion on a Thermo Scientific DELTA V Advantage isotope ratio mass spectrometer (IRMS), operated under a continuous helium flow, and coupled to a COSTECH 4010 elemental analyzer (EA) at the University of California, Riverside. For $\delta^{13}C_{org}$ analysis, ~200 mg of whole-rock powders were decarbonized with 6 N HCl for one hour at 70°C. The solid residue was thoroughly rinsed in deionized water and dried in a clean hood overnight. Small aliquots of decarbonated residues (mostly less than 10 mg) were weighed into tin cups. For $\delta^{15}N_{WR}$ analysis, 20 to 50 mg of powdered whole-rock samples were weighed into tin cups with a blank placed after each sample. Combustion at 1020° utilized ~10 mL of O_2. All isotope data are reported in standard δ–notation relative to V-PDB and Air-N_2 for $\delta^{13}C$ and $\delta^{15}N$, respectively. The isotope measurements were standardized against three in-house standards: Acetanilide from two different batches ($\delta^{13}C$ = -27.9‰, $\delta^{15}N$ = -0.8‰ and $\delta^{13}C$ = -33.7‰, $\delta^{15}N$ = -0.8‰) and Hawaiian Glycine ($\delta^{13}C$ = -36.6‰, $\delta^{15}N$ = 11.3‰), which were calibrated to international reference materials SDO-1 ($\delta^{13}C$ = -30.0‰, $\delta^{15}N$ = -0.8‰; Dennen *et al.*, 2006) and SGR ($\delta^{13}C$ = -29.3‰, $\delta^{15}N$ = 17.4‰; Dennen *et al.*, 2006). Our samples are fully bracketed by the isotopic compositions of the standards (Fig. S1). Replicate analyses for $\delta^{13}C_{org}$ (n = 15) and $\delta^{15}N_{WR}$ (n = 22) yielded an average standard deviation (1σ) better than 0.13 and 0.15‰, respectively. Total organic carbon (TOC) and total nitrogen (TN) abundances were calculated from CO_2 and N_2 peak areas, respectively. The $\delta^{15}N_{WR}$ values are reported only for samples with TN concentrations well above the detection limit. Atomic C:N ratios were calculated by dividing mass ratios (wt.%) by molar masses of 12.01 g/mol for carbon and 14.01 g/mol for nitrogen such that: $C:N_{WR}$ (atomic) = (wt.% C/12.01)/(wt.% N/14.01).

For $\delta^{15}N_{kerogen}$ analysis, a few mg of kerogen were weighed into tin cups and analyzed on a Costech ECS 4010 Elemental Analyzer coupled to a ThermoFinnigan MAT 253 continuous-flow isotope ratio mass spectrometer housed in IsoLab at the Department of Earth & Space Sciences, University of Washington. Combustion utilized 20 mL of O_2 at 1000°C. Analytical blanks were measured and subtracted from data. The resulting isotope data were standardized using in-house standards “GA1” (glutamic acid, $\delta^{15}N$ = -4.6‰), “GA2” (glutamic acid, $\delta^{15}N$ = -5.7‰), and “SA” (dried salmon, $\delta^{15}N$ = +11.3‰) that were calibrated to international reference materials USGS40 and USGS41. The precision and accuracy of $N_{kerogen}$ isotope analysis were better than 0.2‰, based on replicate runs (n = 10).

Results

Redox reconstruction

Iron speciation analysis of shale lithofacies is one of the most widely used methods to evaluate local modern and ancient water-column redox conditions (Chi Fru et al., 2018; Planavsky et al., 2011; Poulton and Canfield, 2011; Poulton and Raiswell, 2002; Sperling et al., 2013). However, formation of iron monosulfides (AVS, pyrrhotite) from pyrite or a conversion of unsulfidized Fe_{HR} to Fe_{PRS} during sediment diagenesis and metamorphic reactions can significantly alter Fe speciation data (Slotznick et al., 2018). Iron sulfides in the Francevillian Group MRS and host sediments are predominantly primary pyrite (Aubineau et al., 2019). The studied samples possess mean Fe_{PRS}/Fe_T ratios of 0.07 ± 0.01 wt.% (Table S2), which is below the average Paleozoic shales (0.39 ± 0.11 wt%; Raiswell *et al.*, 2008). Combined, these data suggest that diagenetic and metamorphic effects are unlikely to have biased our iron speciation results. Petrographic examinations also revealed that the sulfide-bearing sedimentary beds in the FB_2 Member lacked an oxidized iron residue, which is common to weathered horizons (cf. Aubineau *et al.*, 2018, 2020; Fig. 2). Our observations thus suggest that Fe speciation systematics were not appreciably compromised by secondary oxidative weathering, thermal breakdown of pyrite, or late diagenetic processes.

Sediments deposited under anoxic conditions are typically characterized by Fe_{HR}/Fe_T ratios >0.38, while Fe_{HR}/Fe_T ratios less than 0.22 are typical for sediments deposited under oxic conditions. Values between 0.22 and 0.38 are equivocal for interpretation of local redox conditions as they could reflect depositional conditions when sedimentation rate was high or when the transfer of unsulfidized Fe_{HR} to less reactive clay minerals occurred during early to late diagenesis (Poulton et al., 2010). Both mechanisms may mask Fe enrichment under anoxic water-column conditions. If reactive Fe exceeds 38% of the Fe_T and if the Fe_{Py}/Fe_{HR} values are below 0.7-0.8, deposition in ferruginous environment is inferred (Poulton and Canfield, 2011). Values for Fe_{Py}/Fe_{HR} ≥0.7-0.8 typically indicate sulfide-rich (euxinic) water-column conditions. In addition, the Fe_T/Al proxy can also identify Fe enrichments that discriminate between oxic and anoxic depositional environments (Clarkson et al., 2014; Lyons and Severmann, 2006). This ratio is not affected by a transfer of unsulfidized Fe_{HR} to Fe_{PRS} during diagenesis or metamorphism, meaning that the paired use of Fe_T/Al and iron speciation can robustly identify primary redox conditions (Partin et al., 2015; Raiswell et al., 2018). Modern marine sediments deposited under oxic conditions have Fe_T/Al ratio below that of the average upper continental crust (0.55 ± 0.11), and this value can be applied as a threshold for redox evaluation of siliciclastic rocks (Clarkson et al., 2014). Thus, Fe_T/Al values >0.66 (with a confidence threshold of 1σ) suggest local Fe enrichments either under anoxic conditions or due to hydrothermal Fe input. Strong Fe enrichments ($Fe_T/Al > 2$) are often derived from an input of hydrothermal fluids to the water column (Raiswell et al., 2018).

The poorly pyritized and EST samples are predominantly characterized by sub-crustal Fe_T/Al and low Fe_{Py}/Fe_{HR} ratios, with an upsection increase in Fe_{HR} (Fig. 3; Tables S1, S2). In contrast, the pyritized MRS have supra-crustal Fe_T/Al ratios, and high Fe_{HR}/Fe_T and Fe_{Py}/Fe_{HR} values. Both host sandstones and black shales have low Fe_T/Al ratios, whereas the black shales show Fe_{HR}/Fe_T ratios covering the full range of redox conditions, but Fe_{Py}/Fe_{HR} ratios <0.7. The absence of significant, positive Eu anomalies in REE composition of the MRS and black shales indicates that hydrothermal circulation has not strongly affected the depositional site (Aubineau et al., 2020). Instead, variable redox conditions, including oxic, ferruginous, and euxinic, developed during deposition of the MRS and black shales are consistent with localized expression of dissimilatory iron reduction (DIR) and microbial sulfate reduction (MSR) during early diagenesis (Aubineau et al., 2019, 2018) and indicate deposition close to a fluctuating redoxcline.

Redox-sensitive metals

The average Mn concentration in the Francevillian Group FB_2 Member is 0.26 wt.% (Fig. 4, Table S1), more than three times the Mn content of 0.078 wt.% in the upper continental crust (UCC; Rudnick & Gao, 2003). The Mn/Al ratios and EF_{Mn} in both the MRS and host sediments moderately increase upsection (Fig. 4; Table S1). On the other hand, the U/Al, V/Al, and Mo/Al ratios are low for most samples, with values being even lower than those for the UCC. Specifically, the redox-sensitive elements are consistently depleted relative to the UCC in the FB_2 Member host sediments, with the exception of one sandstone sample (mean $EF_{Mo} = 0.7 \pm 0.2$; EF_U and $EF_V = 0.4 \pm 0.1$). The pyrite-bearing MRS display enrichment in Mo due to microbially induced sulfidic conditions that enhanced incorporation of chalcophilic elements (Aubineau et al., 2020).

In the black shale samples, some elements that are known to be associated with organic matter (*e.g.*, Co, Cu, and Ni; Tribovillard *et al.*, 2006) do not show high enrichment relative to the UCC (Table S1). Cobalt is moderately depleted (mean $EF_{Co} = 0.6 \pm 0.8$), while Cu and Ni show only slight mean enrichments ($EF_{Cu} = 1.6 \pm 0.5$; $EF_{Ni} = 1.0 \pm 0.6$, respectively).

Carbon and nitrogen isotope systematics, and phosphorus enrichment

The studied stratigraphic interval shows $\delta^{13}C_{org}$ values similar to the previously published data for the FB_2 Member (Canfield et al., 2013; Gauthier-Lafaye and Weber, 2003), but our whole-rock $\delta^{15}N$ values (Fig. 3; Table S3) differ from those recently reported for the overlying FC Formation by Kipp *et al.* (2018). The average TOC content is 0.28 wt.% for sandstones and

2.21 wt.% for black shales. The TN content for sandstones is close to the detection limit (~0.01 wt.%) and thus must be treated with caution, while that for black shales is nearly constant, with an average of 0.07 wt.%. This difference is accompanied by a change in mean $\delta^{13}C_{org}$ values that average -31.5 ± 1.2‰ (1σ, n = 6) for sandstones and -35.1 ± 0.8‰ (1σ, n = 9) for black shales. Thus, the transition from the FB_{2a} to FB_{2b} unit is marked by a shift towards more negative $\delta^{13}C_{org}$ values. The mean $\delta^{15}N_{WR}$ value for the fine-grained sediments is -0.2 ± 0.4‰ (1σ, n = 8; ranging from -0.8 to 0.6‰), and lacks a distinct stratigraphic trend. Finally, the mean $\delta^{15}N_{kerogen}$ value for the black shales is 1.4 ± 1.0‰ (1σ, n = 5; ranging from -0.2 to +2.3‰).

Carbon and nitrogen contents and isotope values of the different MRS (Fig. 3, Fig. S2; Table S3) reveal that TOC content is high in the poorly pyritized MRS and EST, averaging 6.85 wt.% and 9.78 wt.%, respectively, and decreases, by up to 11 times, to below 0.87 wt.% in the pyritized MRS. Uniform mean TN values of 0.13 and 0.12 wt.% characterize the poorly pyritized MRS and EST, respectively, but TN content of the pyritized MRS is twice lower, with a mean of 0.06 wt.%. The $\delta^{13}C_{org}$ values average -33.9 ± 0.9‰ (1σ, n = 9), -30.5 ± 0.4‰ (1σ, n = 3), and -33.7 ± 0.5‰ (1σ, n = 7) for the poorly pyritized MRS, EST, and pyritized MRS, respectively. The mean $\delta^{13}C_{org}$ values differ between the EST and the pyrite-containing MRS (*i.e.*, poorly pyritized and pyritized MRS) by up to 3.4‰, but without a representative sample size, the significance level of this isotopic heterogeneity remains uncertain. The MRS samples are marked by similar mean $\delta^{15}N_{WR}$ compositions of 0.8 ± 0.6‰ (1σ, n = 9; ranging from -0.1 to +1.9‰), -1.2 ± 2.0‰ (1σ, n = 3; ranging from -3.5 to +0.3‰), and -1.5 ± 1.4‰ (1σ, n = 5; ranging from -3.3 to +0.3‰) for the poorly pyritized MRS, EST, and pyritized MRS, respectively. The $\delta^{15}N_{kerogen}$ values average 2.3 ± 1.0‰ (1σ, n = 5; ranging from +0.9 to +3.6‰) for the pyrite-poor MRS.

The section is characterized by mean P/Ti ratios (ppm/wt.%) of 0.16 and 0.31 for non-pyritized MRS and black shales, respectively (Fig. 3; Table S1). Notably, P is slightly enriched in the FB_{2b} unit (mean EF_P = 1.8 ± 0.2) relative to the UCC.

Discussion

Ocean chemistry during deposition of the Francevillian Group FB_2 Member

To evaluate the redox state of ancient seawater robustly, Fe-based redox proxies should be coupled with other available redox proxies. The sedimentary enrichment of redox-sensitive trace metals is one source of such information, with the potential to reconstruct bottom-water redox conditions. For example, enrichments in U and V preferentially occur under anoxic (euxinic and ferruginous) conditions, while Mo is readily scavenged in anoxic, sulfide-rich (euxinic) waters (Scott et al., 2008; Scott and Lyons, 2012; e.g., Tribovillard et al., 2006).

The Fe- and Mn-rich stratigraphic interval in the upper part of the FB_1 Member has been related to a progressive oxidation of Fe(II) and Mn(II) delivered with deep, anoxic waters upwelled across the chemocline towards shallow, oxygenated waters (Fig. 5a; Ossa Ossa *et al.*, 2018). The Fe- and Mn-rich deposits are thought to be derived from precipitation of Fe(III) and Mn(IV) (oxyhydr)oxides in the water column, followed by conversion to carbonate minerals through early diagenetic dissimilatory reduction of these compounds by microorganisms in association with organic matter oxidation. The moderate Mn enrichment in the FB_2 Member, stratigraphically above the Mn ores of the Upper FB_1 Member, likely indicates a similar process where aqueous Mn(II) was continuously supplied by upwelling deep anoxic waters to the depositional site. Consistent with this interpretation, the FB_2 Member sediments shows iron enrichment in carbonate minerals with Fe_{carb} fraction contributing up to 41% to the total Fe_{HR} reservoir (Table S2). Since the proportion of Fe_{PRS}/Fe_T in studied samples is much lower than the Phanerozoic average, it is unlikely that iron of the carbonate fraction was post-depositionally transferred to the silicate pool, which supports preservation of the original Fe_{HR}/Fe_T signal. In addition, relatively high Mn content in the FB_2 Member could also reflect deposition near the redox boundary (Calvert and Pedersen, 1993). While the seafloor colonization by mat-building cyanobacteria in the MRS and large sulfur isotope fractionations have been used to infer an oxygenated, shallow-marine depositional environment in the photic zone for the FB_2 Member (Aubineau et al., 2018; El Albani et al., 2019; Reynaud et al., 2017), our Fe-speciation data for this interval show evidence for intermittently oxic to anoxic bottom-water conditions likely in proximity to the chemocline (Fig. 5b). Weak to moderate correlations are observed between P and both Ti ($R^2 = 0.17$, $p < 0.08$) and Al ($R^2 = 0.31$, $p < 0.02$) in the studied host sediments (Fig. S3), suggesting that detrital P delivery was not significant, as Ti and Al are usually taken to be detrital tracers (Filippelli et al., 2003; Tribovillard et al., 2006). Moreover, O_2-depleted bottom-waters may limit P burial through reductive dissolution and recycling of primary Fe(III)(oxyhydr)oxides and remineralization of organic matter in sulfate-rich water column and pore-waters (Ingall and Jahnke, 1994). Hence, P input from upwelling waters (Fig. 5b) might be responsible for the minor P enrichment in our black shale samples. Considering the absence of relationship between the sedimentation rate and P and TOC concentrations in modern environments (Ingall and Van Cappellen, 1990), the elevated TOC content in the black shales of the FB_2 Member could reflect high rates of primary organic productivity stimulated by this P input.

While the absence of Mo enrichment is consistent with the Fe-speciation data arguing against persistently euxinic conditions, anoxia cannot account for the lack of U and V enrichment because their accumulation is expected under oxygen-deficient depositional conditions (Tribovillard *et al.*, 2006). In addition, the absence of Co, Cu, and Ni enrichment despite appreciable amounts of organic carbon in the black shales is unusual since these elements are usually enriched in sedimentary rocks in association with organic matter as organometallic complexes (Tribovillard et al., 2006). One possible explanation is that the basinal or global inventory of dissolved redox-sensitive trace metals was depleted. Considering that trace metal reservoir size exerts a first-order control on the magnitude of enrichment (Partin et al., 2013; Scott et al., 2008; Tribovillard et al., 2008), limited metal availability could have played an important role in the absence of Co, Cu, and Ni accumulation. Indeed, trace metals are drawn down almost quantitatively even in some modern anoxic marine environments (*e.g.,* the Black Sea; Algeo & Lyons, 2006), and the same process has been invoked to explain limited trace metal enrichment in the roughly coeval *ca*. 2.0 Ga Zaonega Formation (Kipp et al., 2020). In addition to the redox control on trace metal depletion, basin restriction from the global ocean could have also facilitated depletion of the basinal reservoirs of U, V, Co, Cu, and Ni. The tectonic setting of the Francevillian basin could be invoked to explain basinal restriction from the open ocean or at least to limited connection to the global ocean inventory, especially behind the forebulge (cf. Bankole et al., 2018; Ossa Ossa et al., 2020). Similarly, the absence of wave-related features or storm beds in the FB_2 Member sandstones may indicate that the depositional setting was sheltered by the fault-bounded compartmentalization of the Francevillian basin (Reynaud et al., 2017). It is thus reasonable to assume that geochemical conditions in the Upper FB Formation reflect basin-scale processes. Furthermore, high sedimentation rate of siliciclastic deposits in the FB_2 Member (Reynaud et al., 2017) may have diluted the elemental enrichments (Algeo and Lyons, 2006). However, MRS indicate periods with slow sedimentation rate in the basin and yet show no significant enrichment in U and V. Along these lines, we envisage that these data might reflect benthic productivity and limited export of organic matter with associated trace elements from the photic zone. In light of these considerations, we interpret the observed trends in major and trace element concentrations to record upwelling, anoxic deep waters enriched in Fe, Mn, and P.

C and N isotopic fidelity

The C and N isotope composition of sedimentary rocks can be affected by three main stages of post-depositional alteration, including early diagenesis, late-stage burial diagenesis, and metamorphism (Ader et al., 2016). Therefore, before evaluating organic $\delta^{13}C$ and whole-rock $\delta^{15}N$ signals, we examined whether post-depositional alteration could have overprinted primary signals.

While it has been shown that during the transfer of organic matter from water column to surface sediments the $\delta^{15}N$ signal of primary producers might be altered, settings with high sedimentation and burial rates, short oxygen-exposure time, and high export production tend to faithfully record the isotopic composition of planktonic organisms (Robinson et al., 2012; Tesdal et al., 2013). These characteristics match those inferred for the depositional site of the FB_2 Member, suggesting that the observed N isotope ratios might be reflective of water-column processes; however, a detailed investigation of possible diagenetic effects on C and N isotope ratios is still warranted.

One way to gauge diagenetic reworking of sedimentary organic matter is with C:N ratios. Molar C:N values in modern oceanic phytoplankton range from about 4 to 10 (Ader et al., 2016; Gruber and Galloway, 2008), and the preferential oxidation of labile, N-rich components of marine biomass during its sinking through water column and in sediments can increase the C:N ratio in sedimentary rocks. The analyzed MRS and host sediment samples predominantly show C:N values between 5 and 100 (Fig. 6). These values are similar to those from other Precambrian sedimentary successions that experienced moderate post-depositional thermal alteration (*i.e.* below greenschist facies; Koehler *et al.*, 2017; Kipp *et al.*, 2018; Chang *et al.*, 2019), and are consistent with a moderate diagenetic increase in C:N ratios.

Anoxic diagenetic conditions during deposition of the FB_2 Member are suggested by the occurrence of Fe- and Mn-bearing carbonate minerals formed by microbial reduction of Fe- and Mn-oxyhydroxides (Ossa Ossa et al., 2018) as well as by the abundance of pyrite with early diagenetic S isotope signature (highly negative $\delta^{34}S$ values). Both early and late stage diagenesis under anoxic conditions could slightly modify the $\delta^{15}N_{WR}$ values (Ader et al., 2016). The first step in this process is the degradation of organic-bound N (*i.e.*, remineralization), which releases N as NH_4^+ to pore-waters below the sediment-water interface. Then, NH_4^+ can be incorporated into the interlayers of illite via substitution for potassium cations (Schroeder and McLain, 1998; Williams et al., 1995; Williams and Ferrell Jr, 1991). The phyllosilicate-bound N phases represent up to half of TN content in modern sediments (Müller, 1977). Our dataset shows a strong positive co-variation ($R^2 = 0.74$, $p < 2 \times 10^{-9}$) between TN and K (wt.%), supporting NH_4^+ fixation in K-rich clays during the breakdown of organic matter (Fig. S4a).

Nonetheless, there is no apparent correlation between $\delta^{15}N_{WR}$ and K (wt.%) ($R^2 = 0.11$, $p < 0.12$), which suggests that this diagenetic pathway did not affect the whole-rock $\delta^{15}N$ signal.

Another post-depositional process that elevates C:N ratios and can alter whole-rock C and N isotopic signals is thermal maturation. Specifically, diagenesis and metamorphism can lead to enrichment in heavy C and N isotopes in the remaining reservoir (Bebout & Fogel, 1992; Stüeken *et al.*, 2017a), although the $\delta^{15}N_{WR}$ composition may not significantly change at metamorphic grades up to lower greenschist facies (Ader et al., 2006, 1998; Boudou et al., 2008; Stüeken *et al.*, 2017a). Thermal alteration of organic molecules also drives the depletion of N relative to C (Ader et al., 1998; Bebout and Fogel, 1992). Combined, these processes should result in correlation between $\delta^{13}C_{org}$ and TOC as well as $\delta^{13}C_{org}$ and C:N_{WR}. With increasing burial depth and metamorphism, thermal alteration of organic matter could shift $\delta^{15}N_{WR}$ values up by <1‰ in lower greenschist facies, 1 to 2‰ in greenschist facies, and up to 4‰ in amphibolite facies (Bebout & Fogel, 1992; Stüeken *et al.*, 2017a). The Franceville sub-basin was not affected by metamorphism (Gauthier-Lafaye and Weber, 1989; Ngombi-Pemba et al., 2014), suggesting a maximum increase in whole-rock $\delta^{15}N$ values by less than 1‰ due to burial. Typically, strong co-variation among $\delta^{15}N_{WR}$ and TN, $\delta^{15}N_{WR}$ and C:N, $\delta^{13}C_{org}$ and TOC as well as $\delta^{13}C_{org}$ and C:N_{WR} are taken to indicate metamorphic alteration, as light isotopes are more mobile than heavier ones and N is more mobile than C (Bebout & Fogel, 1992; Stüeken *et al.*, 2017a). In contrast, these correlations are not observed across our Francevillian Group FB_2 Member MRS and host-sediment samples (Fig. S4b), suggesting that thermal maturation did not substantially alter whole-rock C and N isotope signatures. In addition, the $\delta^{15}N_{kerogen}$ values are slightly enriched (on average by +1.6‰) relative to corresponding $\delta^{15}N_{WR}$ values in our samples (Table S3), which is in good agreement with the pattern shown by most of the unmetamorphosed rocks studied by Stüeken *et al.* (2017a). The partitioning between kerogen- and mineral-bound nitrogen within the whole rock under progressive metamorphism is marked by the increase of the isotopic offset between kerogen and whole-rock $\delta^{15}N$ values (Stüeken *et al.*, 2017a; Kipp *et al.*, 2018), with kerogen becoming lighter than the whole-rock, which is not observed in our Francevillian Group FB_2 Member samples, consistent with the unmetamorphosed facies. Thus, we take our C and N isotope data as minimally affected by post-depositional isotopic fractionation.

Interpretation of C and N isotope data for the FB_2 Member

Carbon cycling

Autotrophic microorganisms preferentially incorporate ^{12}C from CO_2, CH_4, or other carbon-bearing organic molecules into their biomass as a function of their carbon fixation pathway, resulting in fractionation of carbon isotopes (Zerkle *et al.*, 2005). Carbon isotope fractionation during primary productivity is also affected by a combination of other factors, including growth rate, dissolved CO_2 level, and the ratio of volume to surface area (Hayes et al., 1999). For the MRS and host sediments, the fractionation of C isotopes from the contemporaneous dissolved inorganic carbon ($\Delta^{13}C$) was on average 35 to 44‰ (1σ confidence interval), using the $\delta^{13}C_{carb}$ within the black shales of the FB Formation with the average of 6.6 ± 1.2‰ (1σ, n = 10; ranging from 5.5 to 9.6‰; El Albani *et al.*, 2010). The latter $\delta^{13}C_{carb}$ values are similar to those of marine carbonates deposited during the LE (Bekker et al., 2008).

The $\delta^{13}C_{org}$ values of the FB_2 Member host sediments are unlikely to reflect the activity of photoautotrophic fixation alone. Instead, they may be pointing to the contribution of organic matter derived from multiple carbon fixation pathways, assuming that the $^{13}C/^{12}C$ ratio of atmospheric CO_2 has not changed significantly through time. Indeed, modern photosynthesizers that assimilate dissolved inorganic carbon in equilibrium with atmospheric CO_2 (with a composition of -7‰) fractionate carbon isotopes by up to about 30‰ through the Calvin–Benson–Bassham cycle (Karhu and Bekker, 2020; Schidlowski, 1987; Zerkle et al., 2005). The substantially larger fractionations between organic and inorganic carbon as recorded by the black shale samples likely reflect secondary productivity in the water column and near the sediment–water interface (cf. Hayes *et al.*, 1999). Specifically, carbon fixation through the reductive acetyl-coenzyme A (=acetyl-CoA) pathway of strictly anaerobic microorganisms, including autotrophic and acetoclastic methanogens, and some sulfate reducers, induces fractionations as large as 40‰, and thus contributing strongly depleted $^{13}C_{org}$ to the sedimentary rock record (Schidlowski, 1987; Zerkle *et al.*, 2005; Stüeken *et al.*, 2017b). However, carbon fixation pathways that fractionate biomass by more than about 40‰ are unknown (Karhu and Bekker, 2020; Schidlowski, 1987; Zerkle et al., 2005). Accordingly, the incorporation of isotopically "superlight" organic carbon into biomass as observed in some of our samples could only be explained by the involvement of secondary productivity, *e.g.* methanotrophy, believed to have been prominent during the deposition of the FB Member (Gauthier-Lafaye and Weber, 2003).

Such microbial activity relies on methane oxidation during which variable electron acceptors are used; both aerobic and anaerobic processes may promote methane oxidation. The large seawater sulfate reservoir at the time of deposition of the Francevillian Group (Bekker et al., 2006; Canfield et al., 2013; Schröder et al., 2008) suggests that the anaerobic oxidation of methane could have occurred with sulfate as an oxidant (*i.e.*, anaerobic oxidation of methane coupled to sulfate reduction). However, we cannot rule out the possibility of aerobic methane oxidation occurring in this setting as well, considering Fe-speciation evidence for intermittently oxic to anoxic bottom-water conditions in the likely proximity of the chemocline. Particularly, Cu is an essential cofactor in the methane monooxygenase, the most active enzyme involved during aerobic biological methane oxidation (Knapp et al., 2007). Given the large amount of land-derived Cu supplied to the oceans during both the GOE and LE (Chi Fru et al., 2016), it is likely that Cu was available to support aerobic methanotrophy at the chemocline (Chi Fru, 2011; Chi Fru et al., 2011). Collectively, highly negative $\delta^{13}C_{org}$ values beyond the range of phototroph-derived organic matter in the studied sediments argue for the addition of isotopically light biomass recording biological methane cycling below or at the redoxcline (Fig. 5b).

The presence of EST, “fairy ring” structures, tufted morphology, and structures interpreted as gas bubbles related to oxygen production in microbial mats suggest that filamentous cyanobacteria were responsible for the development of the Francevillian Group MRS (Aubineau et al., 2019, 2018). However, carbon isotope fractionation (>40‰) in the MRS also points to methane-based metabolism as explained above (Fig. 5b). In this context, the whole range of $\delta^{13}C_{org}$ values in different MRS morphotypes likely reflect the extent to which CO_2 fixation, methane production, and methanotrophy operated in this sedimentary setting.

The absence of extensive pyritization in the pyrite-poor MRS, relative to pyritized MRS, is counterintuitive because a large amount of organic matter is still preserved (Tables S2, S3). However, this could be explained by a change in physical and chemical environmental factors at the FB_{2a}-FB_{2b} unit boundary where high-energy conditions and rapid burial in the depositional setting of the pyrite-poor MRS would have limited the extension of sulfidic pore waters (Aubineau et al., 2020). In addition, the mat thickness seems to play a role in the microbial community assemblage (Suarez et al., 2019), although external environmental parameters (*e.g.*, hydrodynamic regime) also influence the microbial architecture (Battin et al., 2003). The mat thickness allows the expression of distinct redox gradients and internal carbon recycling styles whereby thick mats develop a wide anoxic zone (Suarez et al., 2019). This is consistent with our observations that the poorly pyritized MRS are <0.5 cm thick, whereas the thicker pyritized MRS (Aubineau et al., 2020) promoted the development of the anoxic/sulfidic conditions required to enable strong pyritization. Collectively, the high-energy depositional environment and mat thickness might have been the dominant control on pyrite formation in the FB_2 Member MRS.

Nitrogen cycling

The geochemical data described above indicate the development of intermittently oxic to anoxic bottom-water conditions in likely proximity to the redoxcline during deposition of the FB_2 Member. Well-oxygenated conditions were inferred for the depositional setting of the overlying FC_1 Member (Canfield et al., 2013), in which a pervasive aerobic N cycle has been recognized (Kipp et al., 2018). The latter is characterized by positive $\delta^{15}N$ values (from +4‰ to +7‰) that have been linked to rapid nitrification followed by non-quantitative denitrification in the water column. Such values clearly indicate the predominance of nitrate-using ecosystem that may have comprised both prokaryotes and eukaryotes.

In contrast, the N isotope composition of our samples is consistent with the development of an anaerobic N cycle. $\delta^{15}N$ values between -2‰ and +1‰ usually reflect biological N_2 fixation by cyanobacteria using Mo-bearing nitrogenase (Bauersachs et al., 2009; Carpenter et al., 1997; Minagawa and Wada, 1986; Zhang et al., 2014). At high Fe^{2+} concentrations (>50 nM), fractionations driven by Mo-based diazotrophy can be as large as -4‰ (Zerkle et al., 2008). The very high Fe/Al ratios in the pyritized MRS horizons point to localized Fe-rich water-column conditions during either the mat growth or early diagenesis where DIR and MSR occurred, which may explain their slightly more negative $\delta^{15}N$ values (down to -3.3‰; Fig. 3). Alternative nitrogenase enzymes, in which Fe or V replace Mo at the active site, generate even more ^{15}N-depleted biomass with $\delta^{15}N$ values as low as -8‰ (Stüeken et al., 2016; Zhang et al., 2014). The invariable N isotope composition of the atmosphere over the last 3 Ga ($\delta^{15}N_{air} \approx 0$‰; Sano & Pillinger, 1990; Marty *et al.*, 2013), together with minimal post-depositional alteration, suggest that the $\delta^{15}N_{WR}$ values for the MRS and black shales correspond to the microbial N_2 fixation by Mo-nitrogenase-utilizing cyanobacteria. The N_2 fixation signal recorded by both the MRS and black shales implicates two possible scenarios: the expression of diazotrophy in benthic habitats and in the water column, and/or the contribution of benthically derived biomass (*i.e.* from MRS) to the organic matter content of the black shales (Fig. 5b). The high TOC, TN, and weakly enriched P contents, at least in the pyrite-poor MRS, suggest that productivity was high, which is consistent with nutrient supply with upwelling, anoxic deep-waters, and/or high burial efficiency due to benthic productivity in microbial mats and anoxic water-column conditions. In contrast to other middle Paleoproterozoic depositional settings, including the broadly correlative Zaonega Formation of Karelia, Russia (Kump et al., 2011) and the overlying FC_1 Member of the Franceville sub-basin (Kipp et al., 2018), the FB_2 Member records diazotroph-dominated ecosystem in the coastal area of the upwelling zone where deep, anoxic waters delivered nutrients. Notably, evidence for N_2-fixing cyanobacteria, similar to that producing modern microbial mats (Herbert, 1999;

Woebken et al., 2015), points to processes in the Paleoproterozoic Franceville sub-basin that are reminiscent of modern coastal settings in an oxygen-minimum zone.

One possibility is that the black shales contain organic matter derived from the microbial mats, such that the mat-derived isotopic signatures of N_2 fixation were imprinted onto the black shale facies. The contribution of microbial mats would result in advanced stages of illitization, induced by a biologically mediated K-enrichment in the living mats (Aubineau et al., 2019); this signature was not observed in the FB_{2b} unit black shales. Furthermore, the petrographically distinct morphological features of microbial mat structures were also not observed in the FB_2 Member black shales (Aubineau et al., 2018). Observations from modern sediments have shown that the contribution of isotopically light biomass from *in situ* microbial growth can decrease sedimentary $\delta^{15}N$ values by 1 to 2‰ during anoxic diagenesis (Lehmann et al., 2002). Such a process could potentially explain the near-zero $d^{15}N$ values in the black shales. However, the petrographic and mineralogical evidence seem to suggest that benthically produced organic matter was not a significant contributor to the studied black shales, which instead potentially implicates two distinct organic matter sources for black shales and microbial mats. Hence, the $\delta^{15}N_{WR}$ values of the FB_{2b} unit black shales may reflect the N isotope composition of organic matter delivered from the water column to the sediments. Modern anoxic analogues of a water-column ecosystem dominated by diazotrophs in an otherwise oxygenated and nitrate-replete oceans are known in the Black Sea and Cariaco Basin (Fulton et al., 2012; Thunell et al., 2004). These environments have limited connection to the global ocean, resulting in nitrate depletion. By contrast, the large seawater sulfate reservoir with marine connection in the Francevillian Group FB_2 Member suggests that the depositional environment was not severely restricted with respect to the sulfate reservoir. While it is conceivable that the basin was semi-restricted, leading to depletion of the nitrate reservoir, but not sulfate reservoir due to the high sulfate level at the time of deposition (Bekker et al., 2006; Schröder et al., 2008), allowing negative $\delta^{34}S$ values in pyrite, as is observed in the Black Sea (Lyons, 1997) – it is also possible that another mechanism contributed to the expression of an anaerobic system dominated by biological N_2 fixation.

Nitrogen isotopes along Mesoproterozoic cross-basinal transects have been shown to record aerobic N cycling shoreward, while anaerobic N pathways were restricted to the anoxic deep-water part of the basins (Koehler et al., 2017; Stüeken, 2013). By contrast, the shallow-water depositional setting of the FB_2 Member shows evidence of anaerobic N cycling. Given the high metabolic cost of biological N_2 fixation (16 ATP molecules per molecule of N_2 fixed; Herbert, 1999), the $\delta^{15}N$ values near 0‰ hint that bioavailable nitrogen was indeed scarce in this environment. Considering that the redox potential of Mn(II) oxidation is higher than that for NH_4^+ oxidation, nitrifying microbes could have promoted oxidation of NH_4^+ to NO_2^- and NO_3^- since the relevant redox threshold was crossed, as indicated by the extensive Mn enrichment in the FB Formation. Our data rather suggest that the buildup of a nitrate reservoir was not strong enough to leave a positive isotopic fingerprint (*i.e.*, isotopically heavy residual NO_3^-) via non-quantitative denitrification. In the modern ocean, bioavailable P, N, and Fe are the main nutrient controls on biological productivity in coastal upwelling systems (Capone and Hutchins, 2013). Therefore, P or Fe scarcity could have been the main limiting factor in the production of bioavailable nitrogen. Under widespread anoxic conditions as herein inferred to develop at least episodically in the Franceville sub-basin, it has been hypothesized that phosphorus availability would be restricted via adsorption onto Fe minerals (Reinhard et al., 2017) and high organic carbon burial efficiency because of a scarcity of oxidants for organic remineralization (Kipp and Stüeken, 2017), hampering rates of primary productivity. In contrast, the sizeable seawater sulfate reservoir during deposition of the FB_2 Member sediments would not have limited the P regeneration. We also observe high to moderate TOC concentrations and weak P enrichment in sediments, which contrast with expectations for oligotrophic environments. In modern surface waters of upwelling zones, a shortage of iron induces low N_2 fixation rates (Sohm et al., 2011). Petrographic and geochemical data, combined with Fe speciation results, argue against a significant Fe limitation in the basin during deposition of the FB_2 Member. Molybdenum, one of the essential constituents of the nitrogenase enzyme (Williams and Fraústo da Silva, 2002), could have been a limiting nutrient for biological activity throughout the mid-Proterozoic (Anbar and Knoll, 2002) as it is scavenged from euxinic seawater that episodically and locally developed in upwelling zones in the oceans along continental margins and in intracratonic basins during the mid-Proterozoic. We cannot completely rule out the possibility of Mo limitation during deposition of the FB_2 Member, since low Mo content has been inferred for the Proterozoic oceans (Reinhard et al., 2013; Scott et al., 2008). However, given that Mo-nitrogenase has been operating at Earth's surface since ~3.2 Ga (Stüeken et al., 2015), when Mo was likely more scarce in the marine environment, it is perhaps unlikely that widespread Mo limitation occurred in the mid-Paleoproterozoic, particularly during the "oxygen overshoot" interval during which marine trace metal inventories are thought to have expanded (Bekker and Holland, 2012; Kipp et al., 2017; Partin et al., 2013; Scott et al., 2008).

The threshold at which NH_4^+ is rapidly oxidized via bacterial nitrification is modeled at low micromolar (>1.8 to 11 μM) dissolved oxygen concentrations (Cheng et al., 2019; Fennel et al., 2005; Kipp et al., 2018). Estimates of absolute atmospheric O_2 level in the Paleoproterozoic remain elusive, however, a massive increase in atmospheric O_2 content has been inferred for the LE (Bekker and Holland, 2012; Karhu and Holland, 1996). It seems likely that atmospheric oxygen was maintained at levels high enough to sustain widespread nitrification in the oceans and a substantial dissolved nitrate reservoir during deposition of the FB_2 Member. Thus, if the observed $\delta^{15}N$ values are indicative of locally developed nitrate limitation, this would likely have been a transient state that ultimately yielded to more oxygenated and nitrate-replete conditions.

In this regard, we suggest that the observed nitrate limitation was likely modulated by the basin-scale redox structure in the Franceville sub-basin (Fig. 5). Specifically, the flux of hydrothermally sourced reductants and nutrients may have controlled the redox state at the depositional site for the upper part of the FB_1 Member (Fig. 5a) (Ossa Ossa et al., 2018), involving the upwelling of deep anoxic waters into oxic, shallow-water coastal settings. The large flux of reductants (*e.g.*, Mn and Fe) and nutrients (*e.g.*, P) could have transiently shifted redox conditions to be oxygen-depleted and, thus, triggered denitrification. In modern and ancient coastal upwelling systems with strong inputs of P, intense denitrification and anammox result in a rapid N removal in oxygen-minimum zones, which in turn triggers the surface activity of N_2-fixing photoautotrophs (Capone et al., 1998; Deutsch et al., 2007; Wang et al., 2018). Due to the scarcity of NO_3^- relative to PO_4^{3-}, the N:P ratio of the water column in these settings reaches below the Redfield ratio of 16:1 in phytoplankton biomass (Redfield, 1958). The nitrate limitation in surface waters along upwelling transects appears as a natural consequence of high primary productivity. Furthermore, the loss of fixed nitrogen from the ocean has been proposed as a signature of the oxic-anoxic transition (Fennel et al., 2005). This has also been highlighted in the Ediacaran-Phanerozoic settings whereby enhanced denitrification/anammox and sometimes phosphate addition, together with eustatic fluctuations, would have allowed for the expression of N_2 fixation in shallow depositional environments (Chang et al., 2019; Cremonese et al., 2014; Wang et al., 2013). Further, the nitrate reservoir may be severely depleted if the chemocline was relatively shallow, particularly within the photic zone (Ader et al., 2014; Kipp et al., 2018). Accordingly, introduction of deep anoxic waters developed a redoxcline in the Franceville sub-basin during deposition of the upper part of the FB_1 Member (Fig. 5a). Although the overlying water column should have been more oxygenated with sea-level fall leading to deposition of the FB_2 Member, nitrate limitation developed in surface waters due to enhanced flux of nutrients (*e.g.*, P) with upwelling of anoxic deep-waters in a pattern similar to modern oxygen-minimum zones along continental margins (Fig. 5b) and restricted basins. These conditions ultimately led to the drawdown of the reservoir of bioavailable nitrogen due to high rates of denitrification and anammox activity. The lack of evidence for Mo and P biolimitation, combined with N isotope data indicative of an aerobic N cycle during deposition of the overlying FC_1 Member (Kipp et al., 2018), argue for a local, short-lived N scarcity (Figs. 5b, c).

Implications for primary productivity in the Franceville sub-basin

Our results provide evidence for N_2 fixation both in the MRS and water column in the Franceville sub-basin during deposition of the FB_2 Member. N_2 fixation is commonly observed in microbial mats, however, benthic communities should not significantly contribute to the N budget of the overlying water column (Bebout et al., 1994; Herbert, 1999). Rather, cyanobacterial blooms in the water column strive to replenish the bioavailable N pool (Tyrrell, 1999). The pervasive episodic input of phosphate during deposition of the FB_2 Member suggests that N_2 fixation sustained primary productivity during deposition of the FB_2 Member. Modelling indicates that a high phosphate flux would increase N_2 fixation and bioavailable nitrogen, which in turn invigorates oxygen production and accumulation (Fennel et al., 2005). Although aerobic N cycling during the GOE may have been pervasive as previously suggested (Kipp et al., 2018), our data suggest that regional redox fluctuations – perhaps related to the degree of basinal restriction from the open ocean – controlled the N dynamics in the Franceville sub-basin, which provides insight into heterogeneity of the marine N cycle in the wake of the LE.

Conclusion

The combined study of bottom-water redox proxies and C and N isotopes in the Francevillian Group FB_2 Member MRS and host sediments allowed us to better constrain local redox conditions and microbial biogeochemical cycling at the end of the Lomagundi Event. Our results, summarized in Figure 5, suggest a local, short-lived nitrate scarcity in the water column as well as N_2 fixation by benthic and water-column microbial communities. Importantly, the expression of multiple metabolic C pathways and N_2 fixation in this middle Paleoproterozoic coastal setting points to the existence of biogeochemical C and N cycling in patterns similar to an oxygen-minimum zone developed in a modern coastal upwelling system.

Anoxic deep waters were likely upwelled into oxic, shallow coastal settings across the redoxcline during deposition of the upper part of the FB_1 Member (Fig. 5a). The subsequent sea-level fall and a decrease in a flux of reductants, combined with a continued supply of nutrients, led to increased primary productivity and nitrate limitation in the water column as recorded by the FB_2 Member (Fig. 5b). In the face of this nitrate limitation, diazotrophs sustained primary productivity in surface waters, replenishing the bioavailable N pool (Figs.

5b, c). These redox conditions were superseded by a return to local oxic water-column conditions that allowed the expansion of nitrate-assimilating organisms during deposition of the overlying FC_1 Member. The transient interval dominated by N_2 fixation was thus controlled by the basinal redox structure and flux of reductants, and, to some extent, by the degree of isolation from the global ocean. Although globally oxic conditions prevailed at this time, our results show that regional redox fluctuations led to local nitrate limitation during the LE. Future work should further elucidate the relationship between these local redox conditions, microbial N_2 fixation, and proliferation of the earliest motile macroorganisms.

Acknowledgments

We acknowledge the support of the Gabonese Government, CENAREST, General Direction of Mines and Geology, and Agence Nationale des Parcs Nationaux of Gabon. This work was supported by La Région Nouvelle Aquitaine, the University of Poitiers, Théodore Monod Doctoral School, and the French Embassy in Libreville, Gabon. We are grateful to Prof. P. Mouguiama Daouda, J.C. Balloche, L. White, and R. Oslisly for their support during field trips. For assistance, we acknowledge C. Laforest, C. Lebailly, Y. Lin, L. Magad-Weiss, A. Meunier, A. Oldroyd, P. Recourt, C. Reedman, and X. Tang. J.A. is particularly thankful to T. Lyons for scientific discussions.

References

Ader, M., Boudou, J.-P., Javoy, M., Goffé, B., Daniels, E., 1998. Isotope study on organic nitrogen of Westphalian anthracites from the Western Middle field of Pennsylvania (U.S.A.) and from the Bramsche Massif (Germany). Organic Geochemistry 29, 315–323. https://doi.org/10.1016/S0146-6380(98)00072-2

Ader, M., Cartigny, P., Boudou, J.-P., Oh, J.-H., Petit, E., Javoy, M., 2006. Nitrogen isotopic evolution of carbonaceous matter during metamorphism: Methodology and preliminary results. Chemical Geology 232, 152–169. https://doi.org/10.1016/j.chemgeo.2006.02.019

Ader, M., Sansjofre, P., Halverson, G.P., Busigny, V., Trindade, R.I.F., Kunzmann, M., Nogueira, A.C.R., 2014. Ocean redox structure across the Late Neoproterozoic Oxygenation Event: A nitrogen isotope perspective. Earth and Planetary Science Letters 396, 1–13. https://doi.org/10.1016/j.epsl.2014.03.042

Ader, M., Thomazo, C., Sansjofre, P., Busigny, V., Papineau, D., Laffont, R., Cartigny, P., Halverson, G.P., 2016. Interpretation of the nitrogen isotopic composition of Precambrian sedimentary rocks: Assumptions and perspectives. Chemical Geology 429, 93–110. https://doi.org/10.1016/j.chemgeo.2016.02.010

Algeo, T.J., Lyons, T.W., 2006. Mo-total organic carbon covariation in modern anoxic marine environments: Implications for analysis of paleoredox and paleohydrographic conditions. Paleoceanography 21, PA1016. https://doi.org/10.1029/2004PA001112

Anbar, A.D., Knoll, A.H., 2002. Proterozoic ocean chemistry and evolution: A bioinorganic bridge? Science 297, 1137–1142.

Aubineau, J., El Albani, A., Bekker, A., Chi Fru, E., Somogyi, A., Medjoubi, K., Riboulleau, A., Meunier, A., Konhauser, K.O., 2020. Trace element perspective into the *ca.* 2.1-billion-year-old shallow-marine microbial mats from the Francevillian Group, Gabon. Chemical Geology 543, 119620. https://doi.org/10.1016/j.chemgeo.2020.119620

Aubineau, J., El Albani, A., Bekker, A., Somogyi, A., Bankole, O.M., Macchiarelli, R., Meunier, A., Riboulleau, A., Reynaud, J.-Y., Konhauser, K.O., 2019. Microbially induced potassium enrichment in Paleoproterozoic shales and implications for reverse weathering on early Earth. Nat Commun 10, 2670. https://doi.org/10.1038/s41467-019-10620-3

Aubineau, J., El Albani, A., Chi Fru, E., Gingras, M., Batonneau, Y., Buatois, L.A., Geffroy, C., Labanowski, J., Laforest, C., Lemée, L., Mángano, M.G., Meunier, A., Pierson-Wickmann, A.-C., Recourt, P., Riboulleau, A., Trentesaux, A., Konhauser, K.O., 2018. Unusual microbial mat-related structural diversity 2.1 billion years ago and implications for the Francevillian biota. Geobiology 16, 476–497. https://doi.org/10.1111/gbi.12296

Azziley Azzibrouck, G., 1986. Sédimentologie et géochimie du Francevillien B (protérozoïque inférieur). Métallogénie des gisements de manganèse de Moanda, Gabon. Université Louis Pasteur, Strasbourg.

Bankole, O.M., El Albani, A., Meunier, A., Gauthier-Lafaye, F., 2015. Textural and paleo-fluid flow control on diagenesis in the Paleoproterozoic Franceville Basin, South Eastern, Gabon. Precambrian Research 268, 115–134. https://doi.org/10.1016/j.precamres.2015.07.008

Bankole, O.M., El Albani, A., Meunier, A., Pambo, F., Paquette, J.-L., Bekker, A., 2018. Earth's oldest preserved K-bentonites in the *ca*. 2.1 Ga Francevillian Basin, Gabon. American Journal of Science 318, 409–434. https://doi.org/10.2475/04.2018.02

Bankole, O.M., El Albani, A., Meunier, A., Rouxel, O.J., Gauthier-Lafaye, F., Bekker, A., 2016. Origin of red beds in the Paleoproterozoic Franceville Basin, Gabon, and implications for sandstone-hosted uranium mineralization. American Journal of Science 316, 839–872.

Battin, T.J., Kaplan, L.A., Newbold, J.D., Cheng, X., Hansen, C., 2003. Effects of current velocity on the nascent architecture of stream microbial biofilms. Applied and Environmental Microbiology 69, 5443–5452. https://doi.org/10.1128/AEM.69.9.5443-5452.2003

Bauersachs, T., Schouten, S., Compaoré, J., Wollenzien, U., Stal, L.J., Sinninghe Damsteé, J.S., 2009. Nitrogen isotopic fractionation associated with growth on dinitrogen gas and nitrate by cyanobacteria. Limnol. Oceanogr. 54, 1403–1411. https://doi.org/10.4319/lo.2009.54.4.1403

Bebout, B.M., Paerl, H.W., Bauer, J.E., Canfield, D.E., Des Marais, D.J., 1994. Nitrogen cycling in microbial mat communities: The quantitative importance of N-fixation and other sources of N for primary productivity, in: Stal, L.J., Caumette, P. (Eds.), Microbial Mats Structure, Development and Environmental Significance. Springer, Berlin, Heidelberg, pp. 265–271.

Bebout, G.E., Fogel, M.L., 1992. Nitrogen-isotope compositions of metasedimentary rocks in the Catalina Schist, California: Implications for metamorphic devolatilization history. Geochimica et Cosmochimica Acta 56, 2839–2849. https://doi.org/10.1016/0016-7037(92)90363-N

Bekker, A., El Albani, A., Hofmann, A., Karhu, J.A., Kump, L.R., Ossa Ossa, F., Planavsky, N.J., 2021. The Paleoproterozoic Francevillian succession of Gabon and the Lomagundi-Jatuli event: comment. Géology, in press.

Bekker, A., Holland, H.D., 2012. Oxygen overshoot and recovery during the early Paleoproterozoic. Earth and Planetary Science Letters 317–318, 295–304. https://doi.org/10.1016/j.epsl.2011.12.012

Bekker, A., Holmden, C., Beukes, N.J., Kenig, F., Eglinton, B., Patterson, W.P., 2008. Fractionation between inorganic and organic carbon during the Lomagundi (2.22–2.1 Ga) carbon isotope excursion. Earth and Planetary Science Letters 271, 278–291. https://doi.org/10.1016/j.epsl.2008.04.021

Bekker, A., Karhu, J.A., Kaufman, A.J., 2006. Carbon isotope record for the onset of the Lomagundi carbon isotope excursion in the Great Lakes area, North America. Precambrian Research 148, 145–180. https://doi.org/10.1016/j.precamres.2006.03.008

Bertrand-Sarfati, J., Potin, B., 1994. Microfossiliferous cherty stromatolites in the 2000 Ma Franceville group, Gabon. Precambrian research 65, 341–356.

Bjerrum, C.J., Canfield, D.E., 2004. New insights into the burial history of organic carbon on the early Earth. Geochem. Geophys. Geosyst. 5, Q08001. https://doi.org/10.1029/2004GC000713

Boudou, J.-P., Schimmelmann, A., Ader, M., Mastalerz, M., Sebilo, M., Gengembre, L., 2008.

Organic nitrogen chemistry during low-grade metamorphism. Geochimica et Cosmochimica Acta 72, 1199–1221. https://doi.org/10.1016/j.gca.2007.12.004

Bouton, P., Thiéblemont, D., Gouin, J., Cocherie, A., Guerrot, C., Tegyey, M., Préat, A., Simo Ndounze, S., Kassadou, A.B., Boulingui, B., Ekhogha, H., Moussavou, M., 2009a. Notice explicative de la Carte géologique de la République du Gabon à 1/200,000, feuille Franceville-Boumango, Libreville.

Bouton, P., Thiéblemont, D., Simo Ndounze, S., Goujou, J.C., Kassadou, A.B., Walemba, A., Boulingui, B., Ekhogha, H., Moussavou, M., Lambert, A., Roberts, D., Deschamps, Y., Préat, A., 2009b. Carte géologique de la République du Gabon à 1/200 000, feuille Franceville - Boumango.

Bros, R., Stille, P., Gauthier-Lafaye, F., Weber, F., Clauer, N., 1992. Sm-Nd isotopic dating of Proterozoic clay material: An example from the Francevillian sedimentary series, Gabon. Earth and Planetary Science Letters 113, 207–218.

Calvert, S.E., Pedersen, T.F., 1993. Geochemistry of Recent oxic and anoxic marine sediments: Implications for the geological record. Marine Geology 113, 67–88. https://doi.org/10.1016/0025-3227(93)90150-T

Canfield, D.E., Glazer, A.N., Falkowski, P.G., 2010. The evolution and future of Earth’s nitrogen cycle. Science 330, 192–196. https://doi.org/10.1126/science.1186120

Canfield, D.E., Ngombi-Pemba, L., Hammarlund, E.U., Bengtson, S., Chaussidon, M., Gauthier-Lafaye, F., Meunier, A., Riboulleau, A., Rollion-Bard, C., Rouxel, O., Asael, D., Pierson-Wickmann, A.-C., El Albani, A., 2013. Oxygen dynamics in the aftermath of the Great Oxidation of Earth’s atmosphere. Proceedings of the National Academy of Sciences 110, 16736–16741. https://doi.org/10.1073/pnas.1315570110

Canfield, D.E., Raiswell, R., Westrich, J.T., Reaves, C.M., Berner, R.A., 1986. The use of chromium reduction in the analysis of reduced inorganic sulfur in sediments and shales. Chemical Geology 54, 149–155. https://doi.org/10.1016/0009-2541(86)90078-1

Capone, D.G., Hutchins, D.A., 2013. Microbial biogeochemistry of coastal upwelling regimes in a changing ocean. Nature Geosci 6, 711–717. https://doi.org/10.1038/ngeo1916

Capone, D.G., Subramaniam, A., Montoya, J.P., Voss, M., Humborg, C., Johansen, A.M., Siefert, R.L., Carpenter, E.J., 1998. An extensive bloom of the N_2-fixing cyanobacterium *Trichodesmium erythraeum* in the central Arabian Sea. Marine Ecology Progress Series 172, 281–292.

Carignan, J., Hild, P., Mevelle, G., Morel, J., Yeghicheyan, D., 2001. Routine analyses of trace elements in geological samples using flow injection and low pressure on-line liquid chromatography coupled to ICP-MS: a study of geochemical reference materials BR, DR-N, UB-N, AN-G and GH. Geostandards Newsletter 25, 187–198. https://doi.org/10.1111/j.1751-908X.2001.tb00595.x

Carpenter, E.J., Harvey, H.R., Fry, B., Capone, D.G., 1997. Biogeochemical tracers of the marine cyanobacterium *Trichodesmium*. Deep Sea Research Part I: Oceanographic Research Papers 44, 27–38. https://doi.org/10.1016/S0967-0637(96)00091-X

Chang, C., Hu, W., Wang, X., Huang, K.-J., Yang, A., Zhang, X., 2019. Nitrogen isotope evidence for an oligotrophic shallow ocean during the Cambrian Stage 4. Geochimica et Cosmochimica Acta 257, 49–67. https://doi.org/10.1016/j.gca.2019.04.021

Cheng, C., Busigny, V., Ader, M., Thomazo, C., Chaduteau, C., Philippot, P., 2019. Nitrogen isotope evidence for stepwise oxygenation of the ocean during the Great Oxidation Event. Geochimica et Cosmochimica Acta 261, 224–247. https://doi.org/10.1016/j.gca.2019.07.011

Chi Fru, E., 2011. Copper biogeochemistry: A cornerstone in aerobic methanotrophic bacterial ecology and activity? Geomicrobiology Journal 28, 601–614. https://doi.org/10.1080/01490451.2011.581325

Chi Fru, E., Gray, N.D., McCann, C., Baptista, J. de C., Christgen, B., Talbot, H.M., El Ghazouani, A., Dennison, C., Graham, D.W., 2011. Effects of copper mineralogy and methanobactin on cell growth and sMMO activity in *Methylosinus trichosporium* OB3b. Biogeosciences 8, 2887–2894. https://doi.org/10.5194/bg-8-2887-2011

Chi Fru, E., Kilias, S., Ivarsson, M., Rattray, J.E., Gkika, K., McDonald, I., He, Q., Broman, C., 2018. Sedimentary mechanisms of a modern banded iron formation on Milos Island, Greece. Solid Earth 9, 573–598. https://doi.org/10.5194/se-9-573-2018

Chi Fru, E., Rodríguez, N.P., Partin, C.A., Lalonde, S.V., Andersson, P., Weiss, D.J., El Albani, A., Rodushkin, I., Konhauser, K.O., 2016. Cu isotopes in marine black shales record the Great Oxidation Event. Proc Natl Acad Sci USA 113, 4941–4946. https://doi.org/10.1073/pnas.1523544113

Chi Fru, E., Somogyi, A., El Albani, A., Medjoubi, K., Aubineau, J., Robbins, L.J., Lalonde, S.V., Konhauser, K.O., 2019. The rise of oxygen-driven arsenic cycling at *ca*. 2.48 Ga. Geology 47, 243–246. https://doi.org/10.1130/G45676.1

Clarkson, M.O., Poulton, S.W., Guilbaud, R., Wood, R.A., 2014. Assessing the utility of Fe/Al and Fe-speciation to record water column redox conditions in carbonate-rich sediments. Chemical Geology 382, 111–122. https://doi.org/10.1016/j.chemgeo.2014.05.031

Cremonese, L., Shields-Zhou, G.A., Struck, U., Ling, H.-F., Och, L.M., 2014. Nitrogen and organic carbon isotope stratigraphy of the Yangtze Platform during the Ediacaran–Cambrian transition in South China. Palaeogeography, Palaeoclimatology, Palaeoecology 398, 165–186. https://doi.org/10.1016/j.palaeo.2013.12.016

Dalsgaard, T., Thamdrup, B., Canfield, D.E., 2005. Anaerobic ammonium oxidation (anammox) in the marine environment. Research in Microbiology 156, 457–464. https://doi.org/10.1016/j.resmic.2005.01.011

Dennen, K.O., Johnson, C.A., Otter, M.L., Silva, S.R., Wandless, G.A., 2006. $\delta^{15}N$ and non-carbonate $\delta^{13}C$ values for two petroleum source rock reference materials and a marine sediment reference material. U. S. Geological Survey Open File Report 2006–1071.

Deutsch, C., Sarmiento, J.L., Sigman, D.M., Gruber, N., Dunne, J.P., 2007. Spatial coupling of nitrogen inputs and losses in the ocean. Nature 445, 163–167. https://doi.org/10.1038/nature05392

El Albani, A., Bengtson, S., Canfield, D.E., Bekker, A., Macchiarelli, R., Mazurier, A., Hammarlund, E.U., Boulvais, P., Dupuy, J.-J., Fontaine, C., Fürsich, F.T., Gauthier-Lafaye, F., Janvier, P., Javaux, E., Ossa, F.O., Pierson-Wickmann, A.-C., Riboulleau, A., Sardini, P., Vachard, D., Whitehouse, M., Meunier, A., 2010. Large colonial organisms with coordinated growth in oxygenated environments 2.1 Gyr ago. Nature 466, 100–104. https://doi.org/10.1038/nature09166

El Albani, A., Bengtson, S., Canfield, D.E., Riboulleau, A., Rollion Bard, C., Macchiarelli, R., Ngombi Pemba, L., Hammarlund, E., Meunier, A., Moubiya Mouele, I., Benzerara, K., Bernard, S., Boulvais, P., Chaussidon, M., Cesari, C., Fontaine, C., Chi-Fru, E., Garcia Ruiz, J.M., Gauthier-Lafaye, F., Mazurier, A., Pierson-Wickmann, A.C., Rouxel, O., Trentesaux, A., Vecoli, M., Versteegh, G.J.M., White, L., Whitehouse, M., Bekker, A., 2014. The 2.1 Ga old Francevillian biota: Biogenicity, taphonomy and biodiversity. PLoS ONE 9, e99438. https://doi.org/10.1371/journal.pone.0099438

El Albani, A., Mangano, M.G., Buatois, L.A., Bengtson, S., Riboulleau, A., Bekker, A., Konhauser, K., Lyons, T., Rollion-Bard, C., Bankole, O., Lekele Baghekema, S.G., Meunier, A., Trentesaux, A., Mazurier, A., Aubineau, J., Laforest, C., Fontaine, C., Recourt, P., Chi Fru, E., Macchiarelli, R., Reynaud, J.Y., Gauthier-Lafaye, F., Canfield, D.E., 2019. Organism motility in an oxygenated shallow-marine environment 2.1 billion years ago. Proceedings of the National Academy of Sciences 116, 3431–3436. https://doi.org/10.1073/pnas.1815721116

Farquhar, J., Savarino, J., Airieau, S., Thiemens, M.H., 2001. Observation of wavelength-sensitive mass-independent sulfur isotope effects during SO_2 photolysis: Implications for the early atmosphere. Journal of Geophysical Research 106, 32829–32839. https://doi.org/10.1029/2000JE001437

Fennel, K., Follows, M., Falkowski, P.G., 2005. The co-evolution of the nitrogen, carbon and oxygen cycles in the Proterozoic ocean. American Journal of Science 305, 526–545. https://doi.org/10.2475/ajs.305.6-8.526

Filippelli, G.M., Latimer, J.C., Murray, R.W., Flores, J.-A., 2007. Productivity records from the Southern Ocean and the equatorial Pacific Ocean: Testing the glacial Shelf-Nutrient Hypothesis. Deep Sea Research Part II: Topical Studies in Oceanography 54, 2443–2452. https://doi.org/10.1016/j.dsr2.2007.07.021

Filippelli, G.M., Sierro, F.J., Flores, J.A., Vázquez, A., Utrilla, R., Pérez-Folgado, M., Latimer, J.C., 2003. A sediment–nutrient–oxygen feedback responsible for productivity variations in Late Miocene sapropel sequences of the western Mediterranean. Palaeogeography, Palaeoclimatology, Palaeoecology 190, 335–348. https://doi.org/10.1016/S0031-0182(02)00613-2

Fry, B., Jannasch, H.W., Molyneaux, S.J., Wirsen, C.O., Muramoto, J.A., King, S., 1991. Stable isotope studies of the carbon, nitrogen and sulfur cycles in the Black Sea and the Cariaco Trench. Deep Sea Research Part A. Oceanographic Research Papers 38, S1003–S1019. https://doi.org/10.1016/S0198-0149(10)80021-4

Fulton, J.M., Arthur, M.A., Freeman, K.H., 2012. Black Sea nitrogen cycling and the preservation of phytoplankton $\delta^{15}N$ signals during the Holocene. Global Biogeochem. Cycles 26, GB2030. https://doi.org/10.1029/2011GB004196

Gauthier-Lafaye, F., Weber, F., 2003. Natural nuclear fission reactors: Time constraints for occurrence, and their relation to uranium and manganese deposits and to the evolution of the atmosphere. Precambrian Research 120, 81–100.

Gauthier-Lafaye, F., Weber, F., 1989. The Francevillian (Lower Proterozoic) uranium ore deposits of Gabon. Economic Geology 84, 2267–2285.

Gilleaudeau, G.J., Kah, L.C., 2015. Heterogeneous redox conditions and a shallow chemocline in the Mesoproterozoic ocean: Evidence from carbon–sulfur–iron relationships. Precambrian Research 257, 94–108. https://doi.org/10.1016/j.precamres.2014.11.030

Gruber, N., Galloway, J.N., 2008. An Earth-system perspective of the global nitrogen cycle. Nature 451, 293–296. https://doi.org/10.1038/nature06592

Gumsley, A.P., Chamberlain, K.R., Bleeker, W., Söderlund, U., De Kock, M.O., Larsson, E.R., Bekker, A., 2017. Timing and tempo of the Great Oxidation Event. Proceedings of the National Academy of Sciences 114, 1811–1816. https://doi.org/10.1073/pnas.1608824114

Hannah, J.L., Stein, H.J., Zimmerman, A., Yang, G., Melezhik, V.A., Filippov, M.M., Turgeon, S.C., Creaser, R.A., 2008. Re-Os geochronology of a 2.05 Ga fossil oil field near Shunga, Karelia, NW Russia. Presented at the The 33rd International Geological Congress, Oslo.

Hayes, J.M., Strauss, H., Kaufman, A.J., 1999. The abundance of ^{13}C in marine organic matter and isotopic fractionation in the global biogeochemical cycle of carbon during the past 800 Ma. Chemical Geology 161, 103–125. https://doi.org/10.1016/S0009-2541(99)00083-2

Herbert, R.A., 1999. Nitrogen cycling in coastal marine ecosystems. FEMS Microbiol Rev 23, 563–590. https://doi.org/10.1111/j.1574-6976.1999.tb00414.x

Holland, H.D., 2002. Volcanic gases, black smokers, and the Great Oxidation Event. Geochimica et Cosmochimica Acta 66, 3811–3826.

Horie, K., Hidaka, H., Gauthier-Lafaye, F., 2005. U-Pb geochronology and geochemistry of zircon from the Franceville series at Bidoudouma, Gabon. Presented at the 15th Annual Goldschmidt Conference, Moscow, United States.

Hotinski, R.M., Kump, L.R., Arthur, M.A., 2004. The effectiveness of the Paleoproterozoic biological pump: A δ^{13}C gradient from platform carbonates of the Pethei Group (Great Slave Lake Supergroup, NWT). GSA Bulletin 116, 539–554. https://doi.org/10.1130/B25272.1

Ingall, E., Jahnke, R., 1994. Evidence for enhanced phosphorus regeneration from marine sediments overlain by oxygen depleted waters. Geochimica et Cosmochimica Acta 58, 2571–2575. https://doi.org/10.1016/0016-7037(94)90033-7

Ingall, E.D., Van Cappellen, P., 1990. Relation between sedimentation rate and burial of organic phosphorus and organic carbon in marine sediments. Geochimica et Cosmochimica Acta 54, 373–386. https://doi.org/10.1016/0016-7037(90)90326-G

Kah, L.C., Lyons, T.W., Chesley, J.T., 2001. Geochemistry of a 1.2 Ga carbonate-evaporite succession, northern Baffin and Bylot Islands: implications for Mesoproterozoic marine evolution. Precambrian Research 111, 203–234. https://doi.org/10.1016/S0301-9268(01)00161-9

Karhu, J.A., Bekker, A., 2020. Carbon Isotopes in the Solar System, in: Gargaud, M., Irvine, W.M., Amils, R., Cleaves, H.J., Pinti, D., Cernicharo Quintanilla, J., Viso, M. (Eds.), Encyclopedia of Astrobiology. Springer, Berlin, Heidelberg. https://doi.org/10.1007/978-3-642-27833-4_5395-1

Karhu, J.A., Holland, H.D., 1996. Carbon isotopes and the rise of atmospheric oxygen. Geology 24, 867–870. https://doi.org/10.1130/0091-7613(1996)024<0867:CIATRO>2.3.CO;2

Kipp, M.A., Lepland, A., Buick, R., 2020. Redox fluctuations, trace metal enrichment and phosphogenesis in the ~2.0 Ga Zaonega Formation. Precambrian Research 343, 105716. https://doi.org/10.1016/j.precamres.2020.105716

Kipp, M.A., Stüeken, E.E., 2017. Biomass recycling and Earth's early phosphorus cycle. Sci. Adv. 3, eaao4795. https://doi.org/10.1126/sciadv.aao4795

Kipp, M.A., Stüeken, E.E., Bekker, A., Buick, R., 2017. Selenium isotopes record extensive marine suboxia during the Great Oxidation Event. Proc Natl Acad Sci USA 114, 875–880. https://doi.org/10.1073/pnas.1615867114

Kipp, M.A., Stüeken, E.E., Yun, M., Bekker, A., Buick, R., 2018. Pervasive aerobic nitrogen cycling in the surface ocean across the Paleoproterozoic Era. Earth and Planetary Science Letters 500, 117–126. https://doi.org/10.1016/j.epsl.2018.08.007

Knapp, C.W., Fowle, D.A., Kulczycki, E., Roberts, J.A., Graham, D.W., 2007. Methane monooxygenase gene expression mediated by methanobactin in the presence of mineral copper sources. Proceedings of the National Academy of Sciences 104, 12040–12045. https://doi.org/10.1073/pnas.0702879104

Koehler, M.C., Stüeken, E.E., Kipp, M.A., Buick, R., Knoll, A.H., 2017. Spatial and temporal trends in Precambrian nitrogen cycling: A Mesoproterozoic offshore nitrate minimum. Geochimica et Cosmochimica Acta 198, 315–337. https://doi.org/10.1016/j.gca.2016.10.050

Konhauser, K.O., Lalonde, S.V., Planavsky, N.J., Pecoits, E., Lyons, T.W., Mojzsis, S.J., Rouxel, O.J., Barley, M.E., Rosìere, C., Fralick, P.W., Kump, L.R., Bekker, A., 2011. Aerobic bacterial pyrite oxidation and acid rock drainage during the Great Oxidation Event. Nature 478, 369–373. https://doi.org/10.1038/nature10511

Kroopnick, P.M., 1985. The distribution of ^{13}C of ΣCO_2 in the world oceans. Deep Sea Research 32, 57–84.

Kroopnick, P.M., 1974. Correlations between ^{13}C and ΣCO_2 in surface waters and atmospheric CO_2. Earth and Planetary Science Letters 22, 397–403.

Kump, L.R., Junium, C., Arthur, M.A., Brasier, A., Fallick, A., Melezhik, V., Lepland, A., Crne, A.E., Luo, G., 2011. Isotopic evidence for massive oxidation of organic matter following the Great Oxidation Event. Science 334, 1694–1696. https://doi.org/10.1126/science.1213999

Latimer, J.C., Filippelli, G.M., 2001. Terrigenous input and paleoproductivity in the Southern Ocean. Paleoceanography 16, 627–643. https://doi.org/10.1029/2000PA000586

Lehmann, M.F., Bernasconi, S.M., Barbieri, A., McKenzie, J.A., 2002. Preservation of organic matter and alteration of its carbon and nitrogen isotope composition during simulated and in situ early sedimentary diagenesis. Geochimica et Cosmochimica Acta 66, 3573–3584.

https://doi.org/10.1016/S0016-7037(02)00968-7

Lekele Baghekema, S.G., Lepot, K., Riboulleau, A., Fadel, A., Trentesaux, A., El Albani, A., 2017. Nanoscale analysis of preservation of *ca*. 2.1 Ga old Francevillian microfossils, Gabon. Precambrian Research 301, 1–18. https://doi.org/10.1016/j.precamres.2017.08.024

Luo, G., Junium, C.K., Izon, G., Ono, S., Beukes, N.J., Algeo, T.J., Cui, Y., Xie, S., Summons, R.E., 2018. Nitrogen fixation sustained productivity in the wake of the Palaeoproterozoic Great Oxygenation Event. Nat Commun 9, 978. https://doi.org/10.1038/s41467-018-03361-2

Lyons, T.W., 1997. Sulfur isotopic trends and pathways of iron sulfide formation in upper Holocene sediments of the anoxic Black Sea. Geochimica et Cosmochimica Acta 61, 3367–3382. https://doi.org/10.1016/S0016-7037(97)00174-9

Lyons, T.W., Reinhard, C.T., Planavsky, N.J., 2014. The rise of oxygen in Earth's early ocean and atmosphere. Nature 506, 307–315. https://doi.org/10.1038/nature13068

Lyons, T.W., Severmann, S., 2006. A critical look at iron paleoredox proxies: New insights from modern euxinic marine basins. Geochimica et Cosmochimica Acta 70, 5698–5722. https://doi.org/10.1016/j.gca.2006.08.021

Martin, A.P., Prave, A.R., Condon, D.J., Lepland, A., Fallick, A.E., Romashkin, A.E., Medvedev, P.V., Rychanchik, D.V., 2015. Multiple Palaeoproterozoic carbon burial episodes and excursions. Earth and Planetary Science Letters 424, 226–236. https://doi.org/10.1016/j.epsl.2015.05.023

Marty, B., Zimmermann, L., Pujol, M., Burgess, R., Philippot, P., 2013. Nitrogen Isotopic Composition and Density of the Archean Atmosphere. Science 342, 101–104. https://doi.org/10.1126/science.1240971

Mayika, B.K., Moussavou, M., Prave, A.R., Lepland, A., Mbina, M., Kirsimäe, K., 2020. The Paleoproterozoic Francevillian succession of Gabon and the Lomagundi-Jatuli event. Geology 48. https://doi.org/10.1130/G47651.1

Melezhik, V.A., Fallick, A.E., Rychanchik, D.V., Kuznetsov, A.B., 2005. Palaeoproterozoic evaporites in Fennoscandia: Implications for seawater sulphate, the rise of atmospheric oxygen and local amplification of the $\delta^{13}C$ excursion. Terra Nova 17, 141–148. https://doi.org/10.1111/j.1365-3121.2005.00600.x

Minagawa, M., Wada, E., 1986. Nitrogen isotope ratios of red tide organisms in the East China Sea: A characterization of biological nitrogen fixation. Marine Chemistry 19, 245–259. https://doi.org/10.1016/0304-4203(86)90026-5

Mouélé, I.M., Dudoignon, P., El Albani, A., Meunier, A., Boulvais, P., Gauthier-Lafaye, F., Paquette, J.-L., Martin, H., Cuney, M., 2014. 2.9–1.9 Ga paleoalterations of Archean granitic basement of the Franceville basin (Gabon). Journal of African Earth Sciences 97, 244–260. https://doi.org/10.1016/j.jafrearsci.2014.04.027

Müller, P.J., 1977. C/N ratios in Pacific deep-sea sediments: Effect of inorganic ammonium and organic nitrogen compounds sorbed by clays. Geochimica et Cosmochimica Acta 41, 765–776.

Ngombi-Pemba, L., El Albani, A., Meunier, A., Grauby, O., Gauthier-Lafaye, F., 2014. From detrital heritage to diagenetic transformations, the message of clay minerals contained within shales of the Palaeoproterozoic Francevillian basin (Gabon). Precambrian Research 255, 63–76. https://doi.org/10.1016/j.precamres.2014.09.016

Ossa Ossa, F., Eickmann, B., Hofmann, A., Planavsky, N.J., Asael, D., Pambo, F., Bekker, A., 2018. Two-step deoxygenation at the end of the Paleoproterozoic Lomagundi Event. Earth and Planetary Science Letters 486, 70–83. https://doi.org/10.1016/j.epsl.2018.01.009

Ossa Ossa, F., Hofmann, A., Ballouard, C., Vorster, C., Schoenberg, R., Fiedrich, A., Mayaga-Mikolo, F., Bekker, A., 2020. Constraining provenance for the uraniferous Paleoproterozoic Francevillian Group sediments (Gabon) with detrital zircon geochronology and geochemistry. Precambrian Research 343, 105724. https://doi.org/10.1016/j.precamres.2020.105724

Papineau, D., Purohit, R., Goldberg, T., Pi, D., Shields, G.A., Bhu, H., Steele, A., Fogel, M.L., 2009. High primary productivity and nitrogen cycling after the Paleoproterozoic phosphogenic event in the Aravalli Supergroup, India. Precambrian Research 171, 37–56. https://doi.org/10.1016/j.precamres.2009.03.005

Partin, C.A., Bekker, A., Planavsky, N.J., Lyons, T.W., 2015. Euxinic conditions recorded in the *ca.* 1.93 Ga Bravo Lake Formation, Nunavut (Canada): Implications for oceanic redox evolution. Chemical Geology 417, 148–162. https://doi.org/10.1016/j.chemgeo.2015.09.004

Partin, C.A., Bekker, A., Planavsky, N.J., Scott, C.T., Gill, B.C., Li, C., Podkovyrov, V., Maslov, A., Konhauser, K.O., Lalonde, S.V., Love, G.D., Poulton, S.W., Lyons, T.W., 2013. Large-scale fluctuations in Precambrian atmospheric and oceanic oxygen levels from the record of U in shales. Earth and Planetary Science Letters 369–370, 284–293. https://doi.org/10.1016/j.epsl.2013.03.031

Pavlov, A.A., Kasting, J.F., 2002. Mass-independent fractionation of sulfur isotopes in Archean sediments: Strong evidence for an anoxic Archean atmosphere. Astrobiology 2, 27–41. https://doi.org/10.1089/153110702753621321

Planavsky, N.J., Bekker, A., Hofmann, A., Owens, J.D., Lyons, T.W., 2012. Sulfur record of rising and falling marine oxygen and sulfate levels during the Lomagundi event. Proceedings of the National Academy of Sciences 109, 18300–18305.

Planavsky, N.J., McGoldrick, P., Scott, C.T., Li, C., Reinhard, C.T., Kelly, A.E., Chu, X., Bekker, A., Love, G.D., Lyons, T.W., 2011. Widespread iron-rich conditions in the mid-Proterozoic ocean. Nature 477, 448–451. https://doi.org/10.1038/nature10327

Poulton, S.W., Canfield, D.E., 2011. Ferruginous conditions: A dominant feature of the ocean through Earth's history. Elements 7, 107–112. https://doi.org/10.2113/gselements.7.2.107

Poulton, S.W., Canfield, D.E., 2005. Development of a sequential extraction procedure for iron: Implications for iron partitioning in continentally derived particulates. Chemical Geology 214, 209–221. https://doi.org/10.1016/j.chemgeo.2004.09.003

Poulton, S.W., Fralick, P.W., Canfield, D.E., 2010. Spatial variability in oceanic redox structure 1.8 billion years ago. Nature Geosci 3, 486–490. https://doi.org/10.1038/ngeo889

Poulton, S.W., Raiswell, R., 2002. The low-temperature geochemical cycle of iron: From continental fluxes to marine sediment deposition. American Journal of Science 302, 774–805.

https://doi.org/10.2475/ajs.302.9.774

Préat, A., Bouton, P., Thiéblemont, D., Prian, J.-P., Ndounze, S.S., Delpomdor, F., 2011. Paleoproterozoic high $\delta^{13}C$ dolomites from the Lastoursville and Franceville basins (SE Gabon): Stratigraphic and synsedimentary subsidence implications. Precambrian Research 189, 212–228. https://doi.org/10.1016/j.precamres.2011.05.013

Raiswell, R., Hardisty, D.S., Lyons, T.W., Canfield, D.E., Owens, J.D., Planavsky, N.J., Poulton, S.W., Reinhard, C.T., 2018. The iron paleoredox proxies: A guide to the pitfalls, problems and proper practice. Am J Sci 318, 491–526. https://doi.org/10.2475/05.2018.03

Raiswell, R., Newton, R., Bottrell, S.H., Coburn, P.M., Briggs, D.E.G., Bond, D.P.G., Poulton, S.W., 2008. Turbidite depositional influences on the diagenesis of Beecher's trilobite bed and the hunsrück slate; sites of soft tissue pyritization. American Journal of Science 308, 105–129. https://doi.org/10.2475/02.2008.01

Rasmussen, B., Buick, R., 1999. Redox state of the Archean atmosphere: Evidence from detrital heavy minerals in ca. 3250–2750 Ma sandstones from the Pilbara craton, Australia. Geology 27, 115–118.

Redfield, A.C., 1958. The biological control of chemical factors in the environment. American Scientist 46, 230A, 205–221.

Reinhard, C.T., Planavsky, N.J., Gill, B.C., Ozaki, K., Robbins, L.J., Lyons, T.W., Fischer, W.W., Wang, C., Cole, D.B., Konhauser, K.O., 2017. Evolution of the global phosphorus cycle. Nature 541, 386–389. https://doi.org/10.1038/nature20772

Reinhard, C.T., Planavsky, N.J., Robbins, L.J., Partin, C.A., Gill, B.C., Lalonde, S.V., Bekker, A., Konhauser, K.O., Lyons, T.W., 2013. Proterozoic ocean redox and biogeochemical stasis. Proceedings of the National Academy of Sciences 110, 5357–5362. https://doi.org/10.1073/pnas.1208622110

Reynaud, J.-Y., Trentesaux, A., El Albani, A., Aubineau, J., Ngombi-Pemba, L., Guiyeligou, G., Bouton, P., Gauthier-Lafaye, F., Weber, F., 2017. Depositional setting of the 2.1 Ga Francevillian macrobiota (Gabon): Rapid mud settling in a shallow basin swept by high-density sand flows. Sedimentology 65, 670–701.

Robinson, R.S., Kienast, M., Luiza Albuquerque, A., Altabet, M., Contreras, S., De Pol Holz, R., Dubois, N., Francois, R., Galbraith, E., Hsu, T.-C., Ivanochko, T., Jaccard, S., Kao, S.-J., Kiefer, T., Kienast, S., Lehmann, M., Martinez, P., McCarthy, M., Möbius, J., Pedersen, T., Quan, T.M., Ryabenko, E., Schmittner, A., Schneider, R., Schneider-Mor, A., Shigemitsu, M., Sinclair, D., Somes, C., Studer, A., Thunell, R., Yang, J.-Y., 2012. A review of nitrogen isotopic alteration in marine sediments. Paleoceanography 27, PA4203. https://doi.org/10.1029/2012PA002321

Rudnick, R.L., Gao, S., 2003. Composition of the Continental Crust, in: Rudnick, R.L. (Ed.), The Crust. Elsevier-Pergamon, Oxford, pp. 1–64.

Sano, Y., Pillinger, C.T., 1990. Nitrogen isotopes and N_2/Ar ratios in chests: An attempt to measure time evolution of atmospheric 6^{15}N value. Geochemical Journal 24, 315–325.

Schidlowski, M., 1987. Application of stable carbon isotopes to early biochemical evolution on

Earth. Annual Review of Earth Planetary Sciences 15, 47–72.

Schröder, S., Bekker, A., Beukes, N.J., Strauss, H., van Niekerk, H.S., 2008. Rise in seawater sulphate concentration associated with the Paleoproterozoic positive carbon isotope excursion: Evidence from sulphate evaporites in the ~2.2–2.1 Gyr shallow-marine Lucknow Formation, South Africa. Terra Nova 20, 108–117. https://doi.org/10.1111/j.1365-3121.2008.00795.x

Schroeder, P.A., McLain, A.A., 1998. Illite-smectites and the influence of burial diagenesis on the geochemical cycling of nitrogen. Clay Minerals 33, 539–546. https://doi.org/10.1180/000985598545877

Scott, C., Lyons, T.W., 2012. Contrasting molybdenum cycling and isotopic properties in euxinic versus non-euxinic sediments and sedimentary rocks: Refining the paleoproxies. Chemical Geology 324–325, 19–27. https://doi.org/10.1016/j.chemgeo.2012.05.012

Scott, C., Lyons, T.W., Bekker, A., Shen, Y., Poulton, S.W., Chu, X., Anbar, A.D., 2008. Tracing the stepwise oxygenation of the Proterozoic ocean. Nature 452, 456–459. https://doi.org/10.1038/nature06811

Sigman, D.M., Karsh, K.L., Casciotti, K.L., 2009. Ocean process tracers: Nitrogen isotopes in the ocean, in: Steele, J.H., Turekian, K., Thorpe, S. (Eds.), Encyclopedia of Ocean Sciences. Academic, London, pp. 40–54.

Slotznick, S.P., Eiler, J.M., Fischer, W.W., 2018. The effects of metamorphism on iron mineralogy and the iron speciation redox proxy. Geochimica et Cosmochimica Acta 224, 96–115.

Smittenberg, R.H., Pancost, R.D., Hopmans, E.C., Paetzel, M., Sinninghe Damsté, J.S., 2004. A 400-year record of environmental change in an euxinic fjord as revealed by the sedimentary biomarker record. Palaeogeography, Palaeoclimatology, Palaeoecology 202, 331–351. https://doi.org/10.1016/S0031-0182(03)00642-4

Sohm, J.A., Webb, E.A., Capone, D.G., 2011. Emerging patterns of marine nitrogen fixation. Nat Rev Microbiol 9, 499–508. https://doi.org/10.1038/nrmicro2594

Sperling, E.A., Halverson, G.P., Knoll, A.H., Macdonald, F.A., Johnston, D.T., 2013. A basin redox transect at the dawn of animal life. Earth and Planetary Science Letters 371–372, 143–155. https://doi.org/10.1016/j.epsl.2013.04.003

Stüeken, E.E., 2013. A test of the nitrogen-limitation hypothesis for retarded eukaryote radiation: Nitrogen isotopes across a Mesoproterozoic basinal profile. Geochimica et Cosmochimica Acta 120, 121–139. https://doi.org/10.1016/j.gca.2013.06.002

Stüeken, E.E., Buick, R., Guy, B.M., Koehler, M.C., 2015. Isotopic evidence for biological nitrogen fixation by molybdenum-nitrogenase from 3.2 Gyr. Nature 520, 666–669. https://doi.org/10.1038/nature14180

Stüeken, E.E., Kipp, M.A., Koehler, M.C., Buick, R., 2016. The evolution of Earth's biogeochemical nitrogen cycle. Earth-Science Reviews 160, 220–239. https://doi.org/10.1016/j.earscirev.2016.07.007

Stüeken, E.E., Zaloumis, J., Meixnerová, J., Buick, R., 2017a. Differential metamorphic effects on nitrogen isotopes in kerogen extracts and bulk rocks. Geochimica et Cosmochimica Acta

217, 80–94. https://doi.org/10.1016/j.gca.2017.08.019

Stüeken, E.E., Buick, R., Anderson, R.E., Baross, J.A., Planavsky, N.J., Lyons, T.W., 2017b. Environmental niches and metabolic diversity in Neoarchean lakes. Geobiology 15, 767–783. https://doi.org/10.1111/gbi.12251

Suarez, C., Piculell, M., Modin, O., Langenheder, S., Persson, F., Hermansson, M., 2019. Thickness determines microbial community structure and function in nitrifying biofilms via deterministic assembly. Scientific Reports 9, 5110. https://doi.org/10.1038/s41598-019-41542-1

Tesdal, J.-E., Galbraith, E.D., Kienast, M., 2013. Nitrogen isotopes in bulk marine sediment: linking seafloor observations with subseafloor records. Biogeosciences 10, 101–118. https://doi.org/10.5194/bg-10-101-2013

Thiéblemont, D., Bouton, P., Préat, A., Goujou, J.-C., Tegyey, M., Weber, F., Ebang Obiang, M., Joron, J.L., Treuil, M., 2014. Transition from alkaline to calc-alkaline volcanism during evolution of the Paleoproterozoic Francevillian basin of eastern Gabon (Western Central Africa). Journal of African Earth Sciences 99, 215–227. https://doi.org/10.1016/j.jafrearsci.2013.12.007

Thiéblemont, D., Castaing, C., Billa, M., Bouton, P., Préat, A., 2009. Notice explicative de la carte géologique et des ressources minérales de la République gabonaise à 1/1,000,000.

Thunell, R.C., Sigman, D.M., Muller-Karger, F., Astor, Y., Varela, R., 2004. Nitrogen isotope dynamics of the Cariaco Basin, Venezuela. Global Biogeochem. Cycles 18, GB3001. https://doi.org/10.1029/2003GB002185

Tribovillard, N., Algeo, T.J., Lyons, T., Riboulleau, A., 2006. Trace metals as paleoredox and paleoproductivity proxies: An update. Chemical Geology 232, 12–32. https://doi.org/10.1016/j.chemgeo.2006.02.012

Tribovillard, N., Bout-Roumazeilles, V., Algeo, T., Lyons, T.W., Sionneau, T., Montero-Serrano, J.C., Riboulleau, A., Baudin, F., 2008. Paleodepositional conditions in the Orca Basin as inferred from organic matter and trace metal contents. Marine Geology 254, 62–72. https://doi.org/10.1016/j.margeo.2008.04.016

Tyrrell, T., 1999. The relative infuences of nitrogen and phosphorus on oceanic primary production. Nature 400, 525–531.

Wang, D., Ling, H.-F., Struck, U., Zhu, X.-K., Zhu, M., He, T., Yang, B., Gamper, A., Shields, G.A., 2018. Coupling of ocean redox and animal evolution during the Ediacaran-Cambrian transition. Nat Commun 9, 2575. https://doi.org/10.1038/s41467-018-04980-5

Wang, X., Shi, X., Tang, D., Zhang, W., 2013. Nitrogen isotope evidence for redox variations at the Ediacaran-Cambrian transition in South China. The Journal of Geology 121, 489–502. https://doi.org/10.1086/671396

Wang, X., Zhang, S., Wang, H., Bjerrum, C.J., Hammarlund, E.U., Haxen, E.R., Su, J., Wang, Y., Canfield, D.E., 2017. Oxygen, climate and the chemical evolution of a 1400 million year old tropical marine setting. Am J Sci 317, 861–900. https://doi.org/10.2475/08.2017.01

Warke, M.R., Di Rocco, T., Zerkle, A.L., Lepland, A., Prave, A.R., Martin, A.P., Ueno, Y., Condon, D.J., Claire, M.W., 2020. The Great Oxidation Event preceded a Paleoproterozoic "snowball Earth." Proc Natl Acad Sci USA 117, 13314–13320. https://doi.org/10.1073/pnas.2003090117

Weber, F., 1968. Une série précambrienne du Gabon : le Francevillien. Sédimentologie, géochimie, relations avec les gîtes minéraux associés. Université de Strasbourg, Strasbourg.

Williams, L.B., Ferrell Jr, R.E., 1991. Ammonium substitution in illite during maturation of organic Mmatter. Clays and Clay Minerals 39, 400–408. https://doi.org/10.1346/CCMN.1991.0390409

Williams, L.B., Ferrell Jr, R.E., Hutcheon, I., Bakel, A.J., Walsh, M.M., Krouse, H.R., 1995. Nitrogen isotope geochemistry of organic matter and minerals during diagenesis and hydrocarbon migration. Geochimica et Cosmochimica Acta 59, 765–779. https://doi.org/10.1016/0016-7037(95)00005-K

Williams, R.J.P., Fraústo da Silva, J.J.R., 2002. The Involvement of Molybdenum in Life. Biochemical and Biophysical Research Communications 292, 293–299. https://doi.org/10.1006/bbrc.2002.6518

Woebken, D., Burow, L.C., Behnam, F., Mayali, X., Schintlmeister, A., Fleming, E.D., Prufert-Bebout, L., Singer, S.W., López Cortés, A., Hoehler, T.M., Pett-Ridge, J., Spormann, A.M., Wagner, M., Weber, P.K., Bebout, B.M., 2015. Revisiting N_2 fixation in Guerrero Negro intertidal microbial mats with a functional single-cell approach. ISME J 9, 485–496. https://doi.org/10.1038/ismej.2014.144

Zerkle, A.L., House, C.H., Brantley, S.L., 2005. Biogeochemical signatures through time as inferred from whole microbial genomes. American Journal of Science 305, 467–502. https://doi.org/10.2475/ajs.305.6-8.467

Zerkle, A.L., Junium, C.K., Canfield, D.E., House, C.H., 2008. Production of ^{15}N-depleted biomass during cyanobacterial N_2-fixation at high Fe concentrations. Journal of Geophysical Research 113, G03014. https://doi.org/10.1029/2007JG000651

Zerkle, A.L., Poulton, S.W., Newton, R.J., Mettam, C., Claire, M.W., Bekker, A., Junium, C.K., 2017. Onset of the aerobic nitrogen cycle during the Great Oxidation Event. Nature 542, 465–467. https://doi.org/10.1038/nature20826

Zhang, X., Sigman, D.M., Morel, F.M.M., Kraepiel, A.M.L., 2014. Nitrogen isotope fractionation by alternative nitrogenases and past ocean anoxia. Proceedings of the National Academy of Sciences 111, 4782–4787. https://doi.org/10.1073/pnas.1402976111

Figures

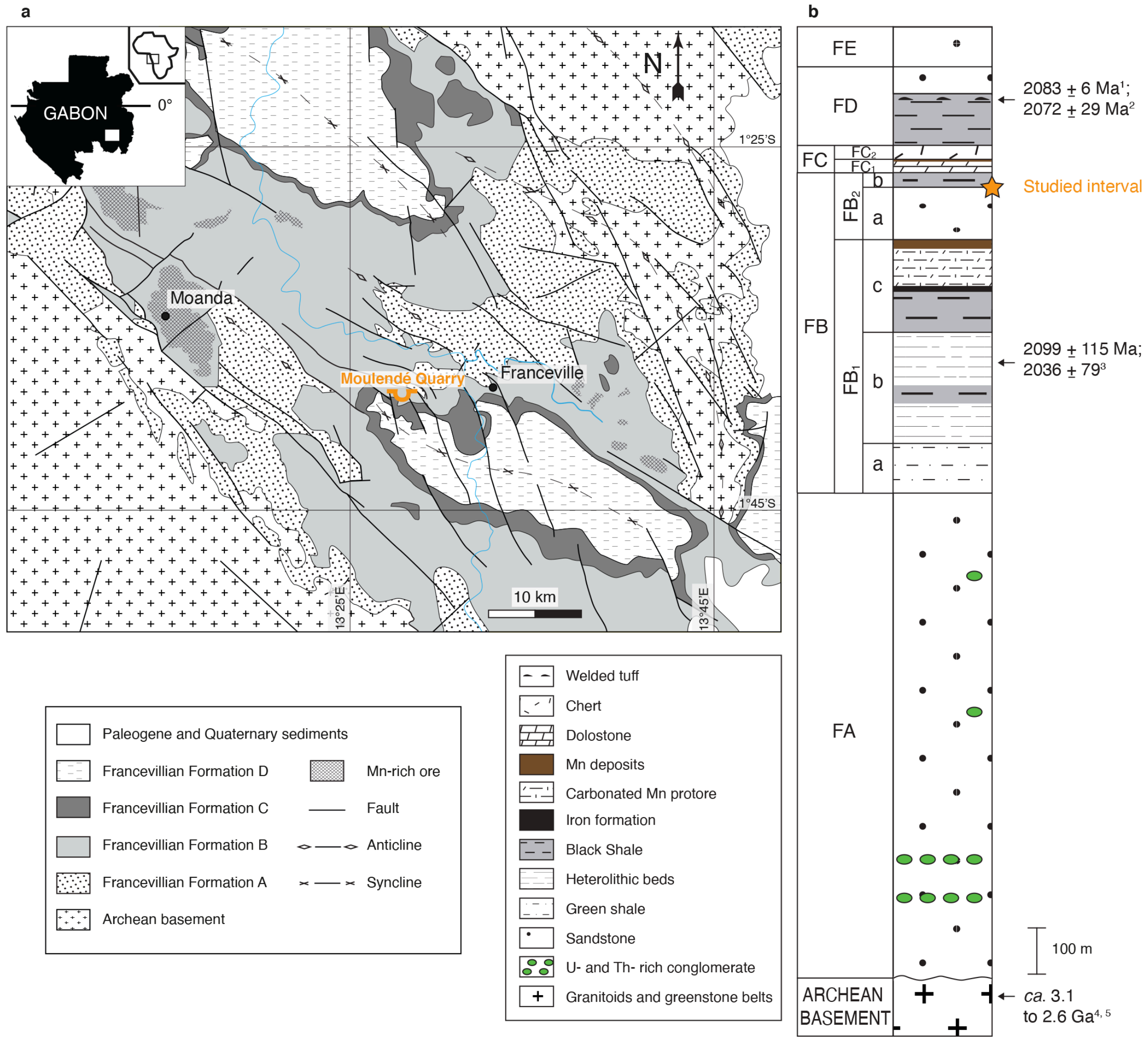

Figure 1: Geological map of the Paleoproterozoic Franceville sub-basin modified from Bouton et al. (2009b) (**a**) and general lithostratigraphic column of the Francevillian Group (**b**). The Moulendé Quarry is the studied area. Sources of ages: [1] - Horie *et al.* (2005); [2] - Thiéblemont *et al.* (2009); [3] - Bros *et al.* (1992); [4] - Mouélé *et al.* (2014); [5] - Ossa Ossa *et al.* (2020). The figure is modified from Aubineau *et al.* (2020).

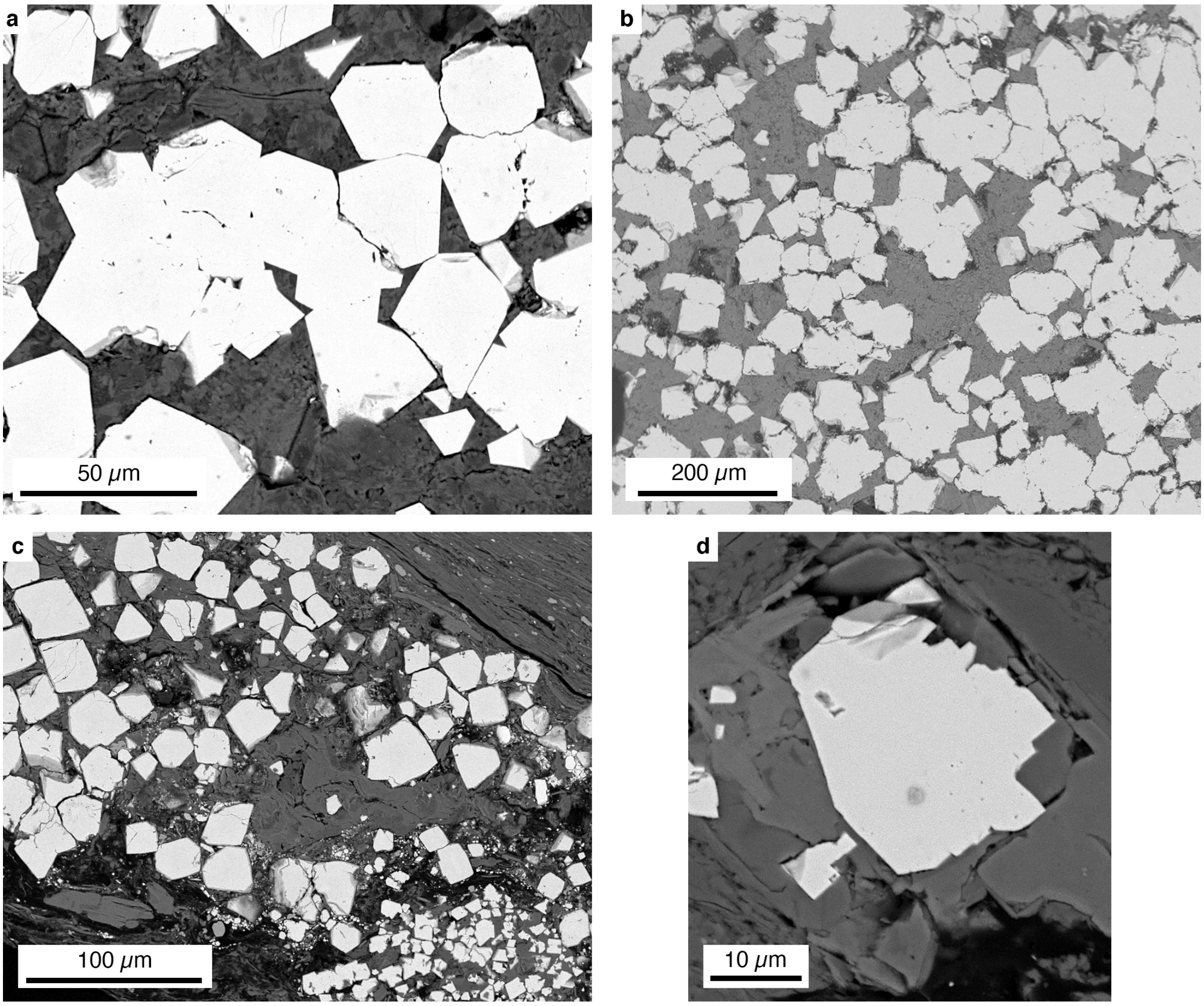

Figure 2: SEM images in backscatter mode of pyrite crystals showing the absence of alteration and recrystallization. **a** and **b**, Pyritized MRS. **c**, Poorly pyritized MRS. **d**, Black shales.

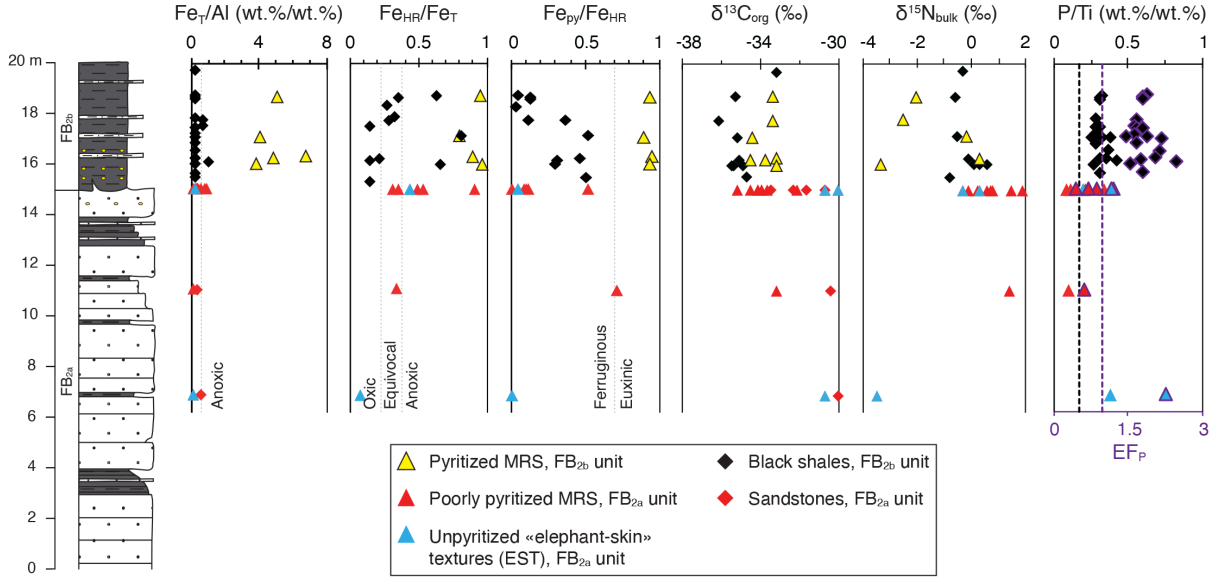

Figure 3: Geochemical data for the MRS and host sediments plotted along the lithostratigraphic profile of the studied sequence of the FB$_2$ Member. Grey, black, and purple vertical lines represent redox boundaries as in Raiswell *et al*. (2018), the UCC value from Rudnick & Gao (2003), and the EF$_P$ for the UCC is 1, respectively. Fe/Al for the UCC is shown with grey dash line.

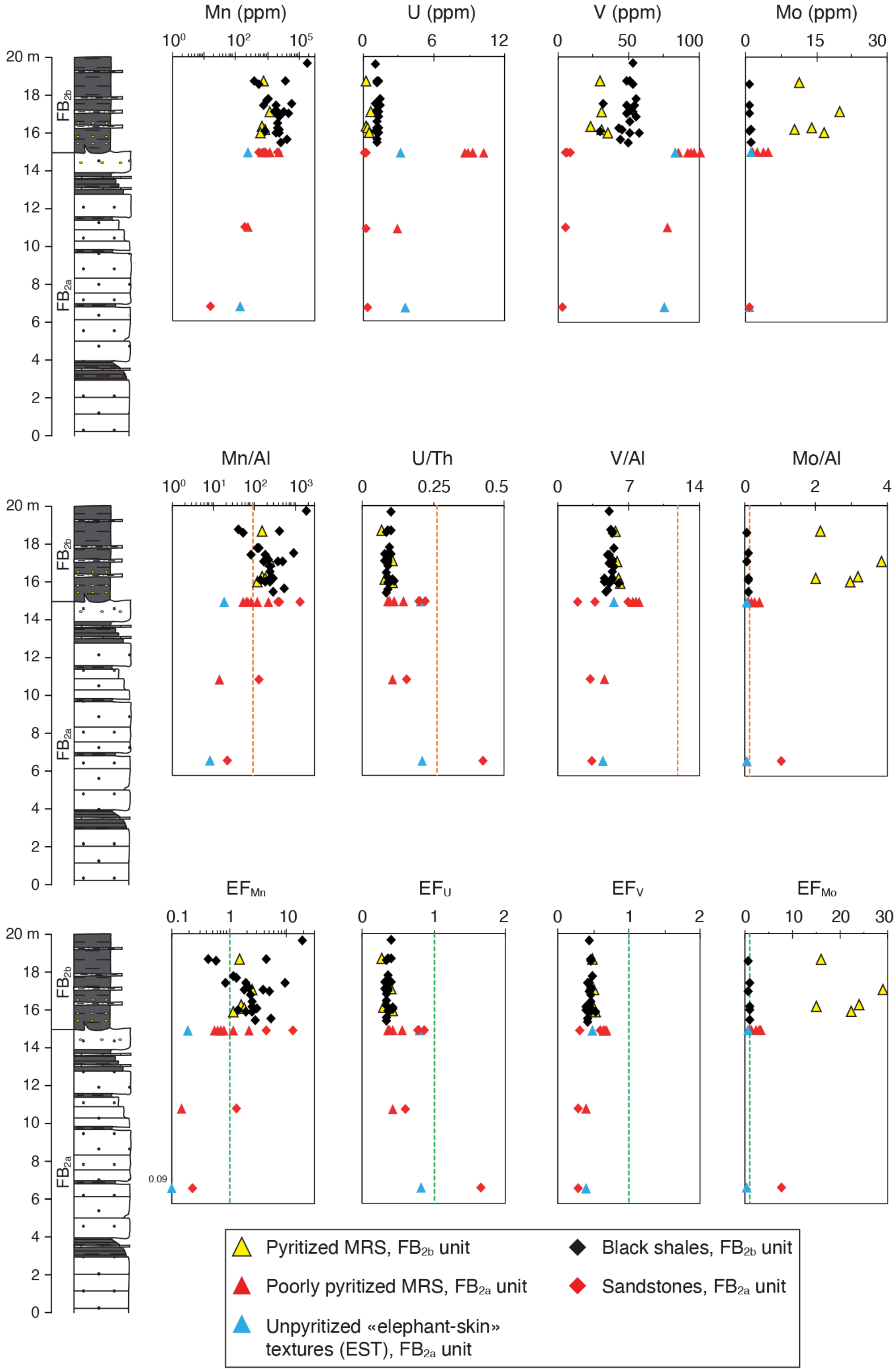

Figure 4: Data for redox-sensitive metals from the MRS and host sediments plotted along the lithostratigraphic profile of the studied sequence of the FB_2 Member. Orange and green vertical lines correspond to the UCC ratio from Rudnick & Gao (2003) and the EF for the UCC of 1, respectively. The Mn/Al, V/Al, and Mo/Al ratios are expressed in ppm/wt.%.

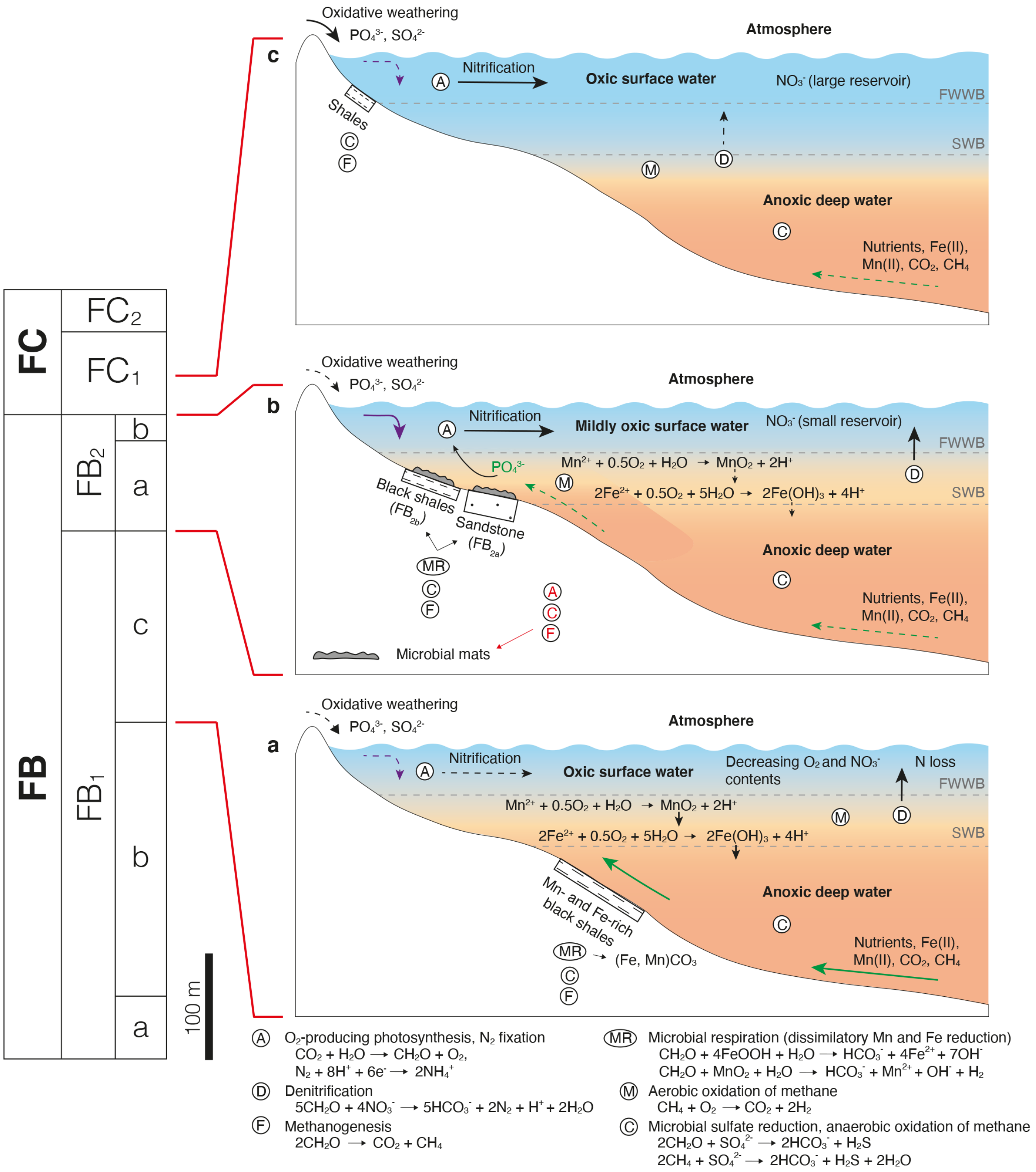

Figure 5: Proposed reconstruction of redox conditions during deposition of the Upper Francevillian Group at the end of the LE. **a** - During deposition of the upper part of the FB_1 Member, upwelling of reducing fluids into oxic, shallow coastal area (Ossa Ossa et al., 2018) likely led to the first step of deoxygenation and decrease in bioavailable nitrate. **b** - During deposition of the FB_2 Member, bioavailable nitrate was scarce. Upwelling brought anoxic bottom seawater rich in Fe, Mn, and P. Phosphorous availability in surface waters along with limitation of bioavailable nitrate resulted in high primary productivity fueled by diazotrophs, which partially replenished bioavailable nitrogen. Microbial mats flourished and also fixed nitrogen. Sandstones were delivered with high-density gravity currents to the mud-rich

depositional environment (Reynaud et al., 2017). The FB_2 Member is, therefore, interpreted as a forced regressive system tract. **c** - Recovery in nitrate availability during deposition of the lower part of FC_1 Member (cf. Kipp *et al.*, 2018) indicates the transient nature of nitrate limitation during deposition of the FB_2 Member that was modulated by the redox structure of the Francevillian basin, degree of isolation from the ocean, and flux of reductants. FWWB, fair-weather wave base; SWB, storm wave base. Purple and green arrows indicate the sediment supply and the upwelling system, respectively. Processes were less intense when arrows are dotted.

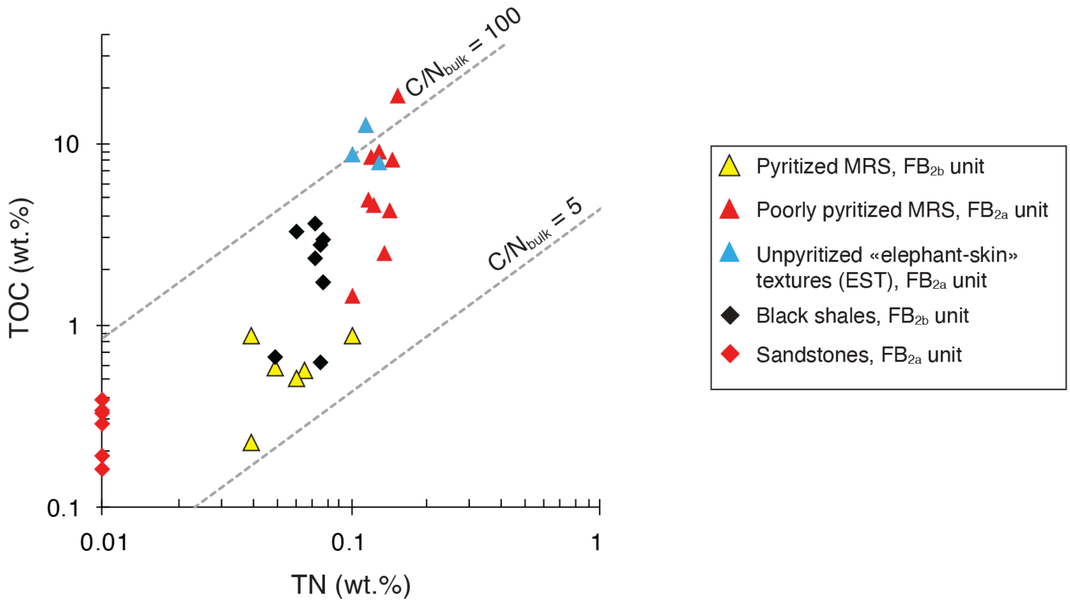

Figure 6: Cross plot of total organic carbon versus total nitrogen for MRS and host sediments. Dotted lines show molar C:N ratios of 5 and 100. The molar C:N values of modern marine phytoplankton range from 4 to 10 (Ader et al., 2016; Canfield et al., 2010). Remineralization of biomass in the water column and during diagenesis increases the C:N ratios.

SUPPLEMENTARY INFORMATION

SUPPLEMENTARY FIGURES

FIGURE S1

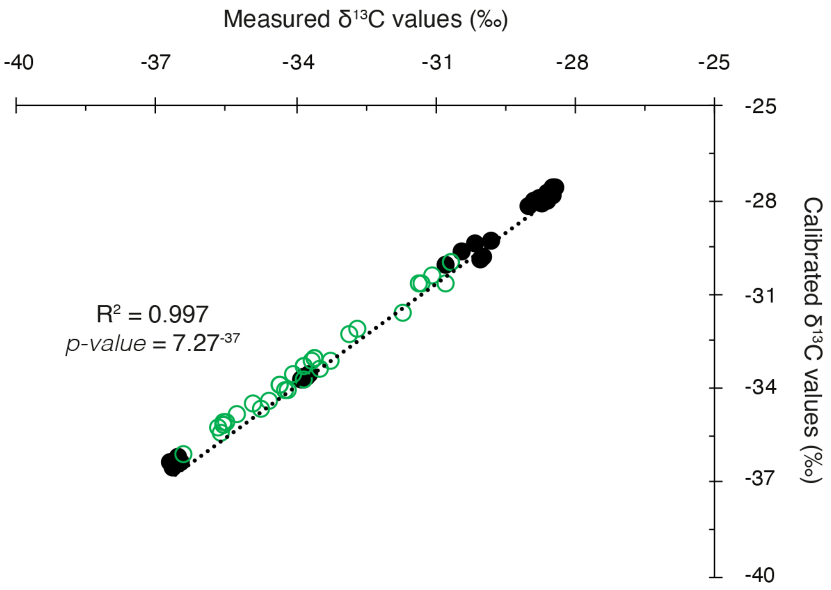

Figure S1: Relationship between measured and calibrated $\delta^{13}C_{org}$ values for standards (2 batches of Acetanilide, Hawaiian Glycine, and SDO-1) and FB_2 Member MRS and host sediments. Filled symbols denote standards and unfilled symbols represent the studied samples.

FIGURE S2

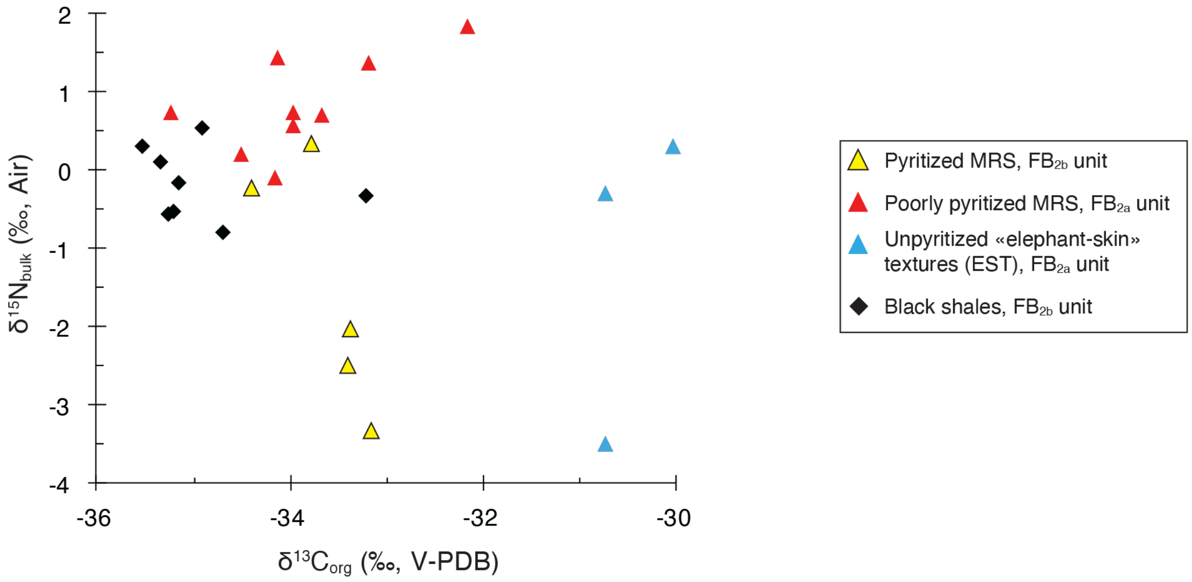

Figure S2: $\delta^{15}N_{WR}$ values plotted against $\delta^{13}C_{org}$ values for the MRS and black shales of the FB$_2$ Member of the Franceville sub-basin.

FIGURE S3

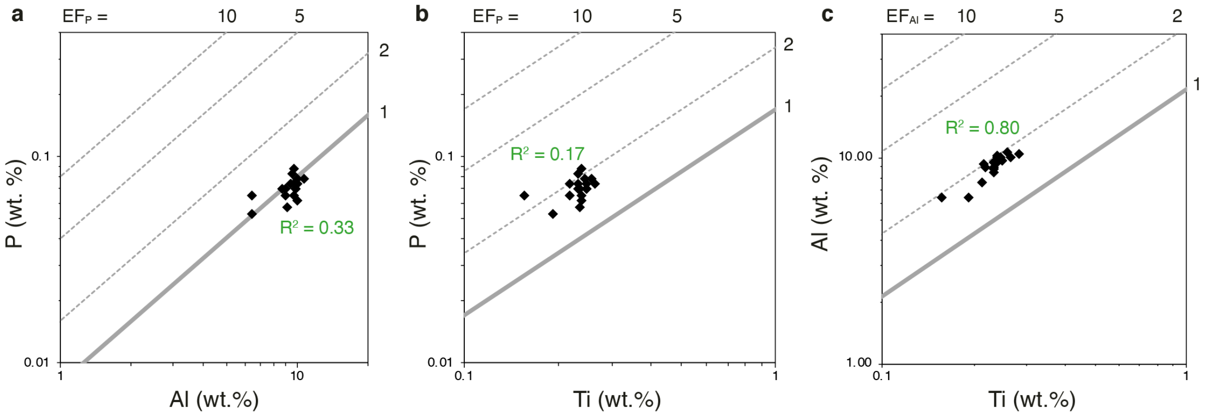

Figure S3: Co-variation among whole-rock phosphorus and detrital indicators as well as Ti and Al in the FB$_{2b}$ unit black shales. **a**, P vs. Al. **b**, P vs. Ti. **c**, Al vs. Ti.

FIGURE S4

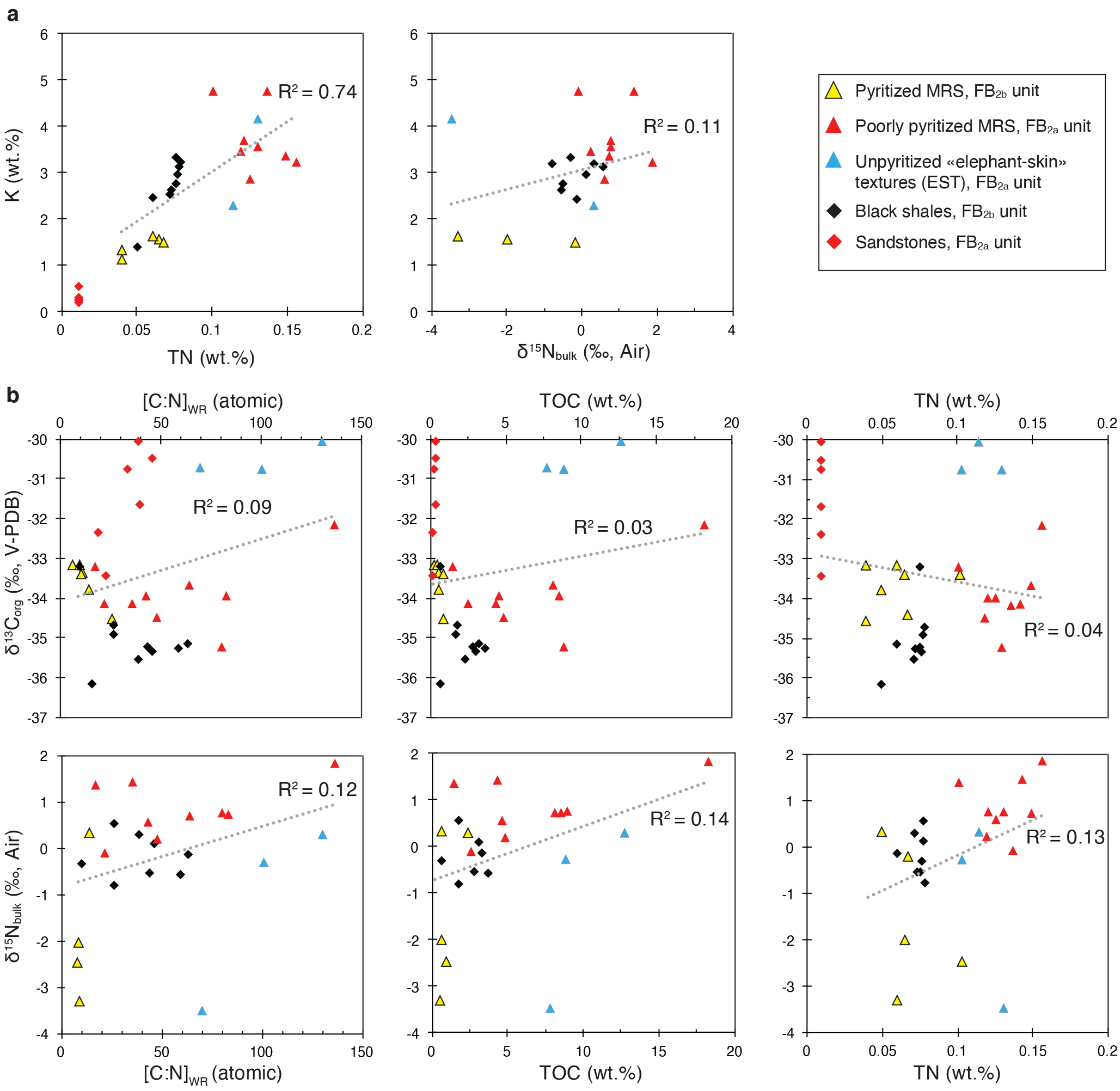

Figure S4: Cross-plots for assessment of data fidelity. **a**, Cross-plots of K content with TN and $\delta^{15}N_{WR}$ values. **b**, Geochemical data for all whole-rock analyses for the FB_2 Member.

SUPPLEMENTARY TABLES

TABLE S1. Whole-rock composition of major and trace elements for all samples in this study.

Formation	Lithology	Sample ID	Height m	Al (wt. %)	Fe$_T$ (wt. %)	Mn (wt. %)	K (wt. %)	Ti (wt. %)	P ppm	Co ppm	Cu ppm	Ni ppm	Mo ppm	Th ppm	U ppm	V ppm	Fe/Al	Mn/Al* 95†	P/Al 0.008†	P/Ti** 0.17†	Mo/Al 0.13†	U/Th 0.26	V/Al 11.89†	EF$_{Mn}$	EF$_P$	EF$_{Co}$	EF$_{Cu}$	EF$_{Ni}$	EF$_{Mo}$	EF$_U$	EF$_V$
FB2b	Pyritized MRS	FPS_s5-mat§	18.70	5.35	26.86	0.08	1.56	0.08	b.d.	252.90	147.70	738.80	11.40	4.24	0.29	30.19	5.02	149.19	b.d.	b.d.	2.13	0.07	5.64	1.57	b.d.	22.29	8.04	23.96	15.80	0.27	0.47
		DB_s4-mat§	17.10	5.14	20.80	0.12	1.50	0.11	b.d.	326.20	192.10	589.20	19.81	6.03	0.62	30.27	4.05	241.91	b.d.	b.d.	3.85	0.10	5.89	2.55	b.d.	29.91	10.88	19.89	28.57	0.40	0.50
		FPS_s4-mat§	16.30	4.37	29.02	0.07	1.11	0.07	b.d.	192.60	82.20	587.60	13.94	3.70	0.30	23.48	6.64	150.75	b.d.	b.d.	3.19	0.08	5.37	1.59	b.d.	20.76	5.47	23.31	23.63	0.31	0.45
		FPS_s3-mat§	16.20	5.09	24.68	0.09	1.34	0.09	b.d.	144.20	99.99	547.30	10.23	4.64	0.36	30.67	4.85	181.06	b.d.	b.d.	2.01	0.08	6.02	1.91	b.d.	13.35	5.72	18.65	14.89	0.30	0.51
		DB_s3-mat§	16.00	5.56	20.89	0.06	1.63	0.09	b.d.	99.42	25.61	176.60	16.62	4.80	0.52	34.78	3.33	115.94	b.d.	b.d.	2.99	0.11	6.26	1.22	b.d.	8.43	1.34	5.51	22.16	0.42	0.53
	Black shales	WS_s2-sed	19.70	10.40	1.90	1.85	3.34	0.28	b.d.	11.12	13.38	51.38	b.d.	10.0	1.02	53.37	0.18	1777.46	b.d.	b.d.	b.d.	0.10	5.13	18.71	b.d.	0.50	0.37	0.86	b.d.	0.40	0.43
		GFB2-R6 1	18.75	9.56	1.92	0.04	2.91	0.23	742.25	4.54	37.53	45.31	b.d.	13.47	1.20	50.49	0.20	40.85	0.008	0.32	b.d.	0.09	5.28	0.43	1.87	0.22	1.14	0.82	b.d.	0.35	0.44
		FPS_s5-sed§	18.70	8.85	1.67	0.37	2.63	0.23	698.59	4.17	53.10	29.01	b.d.	13.1	1.32	48.28	0.19	413.10	0.008	0.30	b.d.	0.10	5.46	4.35	1.76	0.22	1.75	0.57	b.d.	0.39	0.46
		AFBSO-12#	18.60	9.87	2.41	0.05	3.01	0.25	742.25	8.89	56.63	60.68	0.76	14.4	1.21	52.97	0.24	54.94	0.008	0.30	0.08	0.08	5.37	0.58	1.77	0.42	1.67	1.07	0.57	0.33	0.45
		AFBSO-11#	18.30	-	-	-	-	-	-	-	-	-	-	-	-	-	-	-	-	-	-	-	-	-	-	-	-	-	-	-	-
		AFBSO-10#	17.90	-	-	-	-	-	-	-	-	-	-	-	-	-	-	-	-	-	-	-	-	-	-	-	-	-	-	-	-
		GFB2-R14 1	17.80	9.86	1.98	0.11	3.05	0.25	698.59	5.05	69.14	46.54	b.d.	15.55	1.43	55.00	0.20	113.03	0.007	0.28	b.d.	0.09	5.58	1.19	1.67	0.24	2.04	0.82	b.d.	0.36	0.47
		LP_s4-sed	17.75	7.61	5.05	0.10	1.40	0.21	b.d.	-	-	-	-	-	-	-	0.66	128.02	b.d.	b.d.	-	-	-	1.35	b.d.	-	-	-	-	-	-
		AFBSO-09#	17.50	6.38	4.55	0.57	1.22	0.19	523.94	20.14	34.59	83.16	0.76	10.8	1.08	32.39	0.71	898.49	0.008	0.27	0.12	0.10	5.08	9.46	1.60	1.49	1.58	2.26	0.88	0.39	0.43
		GFB2-R18 1	17.48	9.70	2.07	0.08	3.00	0.25	698.59	14.80	63.80	67.01	b.d.	16.37	1.31	48.44	0.21	84.91	0.007	0.28	b.d.	0.08	4.99	0.89	1.65	0.72	1.92	1.20	b.d.	0.31	0.42
		GFB2-R11 1	17.45	10.60	1.70	0.20	3.36	0.26	785.92	6.39	55.12	42.32	b.d.	16.11	1.43	53.47	0.16	189.03	0.007	0.31	b.d.	0.09	5.05	1.99	1.79	0.28	1.51	0.69	b.d.	0.35	0.42
		GFB2-R16 1	17.20	9.59	1.66	0.20	2.89	0.24	654.93	4.57	73.91	37.95	b.d.	13.60	1.18	51.51	0.17	207.67	0.007	0.27	b.d.	0.09	5.37	2.19	1.61	0.22	2.25	0.69	b.d.	0.34	0.45
		DB_s4-sed§	17.10	9.04	1.96	0.34	2.75	0.23	567.61	4.18	58.04	42.64	b.d.	13.5	1.24	49.54	0.22	379.31	0.006	0.24	b.d.	0.09	5.48	3.99	1.43	0.22	1.87	0.82	b.d.	0.35	0.46
		B01 1	17.10	9.97	1.98	0.17	3.07	0.24	785.92	7.83	44.39	52.73	b.d.	15.73	1.25	52.79	0.20	170.26	0.008	0.32	b.d.	0.08	5.29	1.79	1.88	0.37	1.30	0.92	b.d.	0.31	0.44
		GFB2-R19 1	17.05	9.64	2.05	0.47	3.04	0.24	873.24	13.54	8.83	54.39	0.66	12.68	1.15	48.75	0.21	491.54	0.009	0.37	0.07	0.09	5.06	5.17	2.17	0.66	0.27	0.98	0.51	0.35	0.42
		GFB2-R12 1	16.85	9.99	1.71	0.23	3.10	0.26	742.25	8.93	53.92	47.24	b.d.	14.78	1.29	54.88	0.17	232.40	0.007	0.28	b.d.	0.09	5.50	2.45	1.66	0.42	1.57	0.82	b.d.	0.34	0.46
		GFB2-R13 1	16.55	9.43	1.85	0.22	2.89	0.23	829.58	6.04	49.28	37.86	b.d.	14.30	1.21	50.44	0.20	235.65	0.009	0.36	b.d.	0.08	5.35	2.48	2.10	0.30	1.52	0.70	b.d.	0.33	0.45
		JN35 1	16.25	9.28	1.78	0.22	2.82	0.22	742.25	4.64	35.77	39.96	b.d.	13.25	1.15	43.30	0.19	238.79	0.008	0.34	b.d.	0.09	4.67	2.51	2.01	0.24	1.12	0.75	b.d.	0.34	0.39
		FPS_s3-sed§	16.20	8.51	1.64	0.24	2.45	0.23	698.59	3.94	62.10	26.18	0.85	12.0	1.28	45.40	0.19	282.04	0.008	0.30	0.10	0.11	5.33	2.97	1.75	0.22	2.12	0.53	0.74	0.41	0.45
		AFBSO-06#	16.10	6.37	6.21	0.09	1.12	0.16	654.93	49.92	28.16	115.10	0.72	9.5	1.02	29.13	0.97	133.77	0.010	0.42	0.11	0.11	4.57	1.41	2.46	3.69	1.29	3.13	0.84	0.42	0.38
		DB_s2-sed§	16.00	9.45	1.50	0.23	2.98	0.24	b.d.	3.43	57.57	30.55	b.d.	14.5	1.32	57.54	0.16	244.06	b.d.	b.d.	b.d.	0.09	6.09	2.57	b.d.	0.17	1.77	0.56	b.d.	0.35	0.51
		FR_s1sed§	16.00	9.98	1.65	0.19	3.14	0.24	611.27	5.30	57.01	33.45	b.d.	12.8	1.24	50.73	0.17	189.04	0.006	0.26	b.d.	0.10	5.08	1.99	1.51	0.25	1.66	0.58	b.d.	0.38	0.43
		GFB2-R4 1	15.65	8.88	1.99	0.45	2.73	0.22	654.93	5.74	58.39	49.36	b.d.	13.61	1.18	43.78	0.22	506.93	0.007	0.30	b.d.	0.09	4.93	5.34	1.76	0.30	1.91	0.96	b.d.	0.34	0.41
		MLS_s9-sed§	15.50	10.13	2.12	0.28	3.21	0.24	b.d.	12.75	62.95	58.74	0.93	13.6	1.13	49.27	0.21	280.26	b.d.	b.d.	0.09	0.08	4.86	2.95	b.d.	0.59	1.81	1.01	0.68	0.32	0.41
		AFBSO-05#	15.30	-	-	-	-	-	-	-	-	-	-	-	-	-	-	-	-	-	-	-	-	-	-	-	-	-	-	-	-
FB2a	Pyrite-poor MRS	MLS_s1-mat§	15.0	11.96	9.17	0.25	3.46	1.66	2445.07	45.86	208.60	228.80	4.76	77.88	8.54	96.43	0.77	207.66	0.020	0.15	0.40	0.11	8.07	2.19	0.86	1.81	5.08	3.32	2.95	0.43	0.68
		MLS_s2-mat§	15.0	12.34	6.61	0.08	3.36	2.03	1571.83	48.40	155.50	223.90	3.66	111.20	10.16	91.74	0.54	61.42	0.013	0.08	0.30	0.09	7.44	0.65	0.45	1.85	3.67	3.15	2.20	0.36	0.63
		EST_s3-mat§	15.0	14.78	2.43	0.03	2.31	0.22	436.62	4.59	12.89	75.91	0.85	15.571	3.19	82.74	0.16	17.87	0.003	0.20	0.06	0.20	5.60	0.19	1.16	0.15	0.25	0.89	0.42	0.80	0.47
		MLS_s6-mat§	15.0	10.94	9.33	0.12	2.87	1.40	2838.03	32.23	115.40	167.30	4.63	64.95	9.20	84.62	0.85	113.51	0.026	0.20	0.42	0.14	7.74	1.19	1.19	1.39	3.07	2.65	3.14	0.55	0.65
		MLS_s4-mat§	15.0	12.59	3.98	0.08	3.68	1.66	2226.76	15.79	121.10	134.20	1.44	99.45	8.92	93.92	0.32	67.49	0.018	0.13	0.11	0.09	7.46	0.71	0.79	0.59	2.80	1.85	0.85	0.35	0.63
		MLS_s5-mat§	15.0	12.99	4.48	0.07	3.56	2.03	2139.44	13.24	64.23	119.40	2.29	96.85	9.20	99.93	0.34	52.00	0.016	0.11	0.18	0.10	7.69	0.55	0.62	0.48	1.44	1.59	1.31	0.37	0.65
		MLS_s10-mat	15.0	12.54	0.86	b.d.	3.22	1.73	b.d.	-	-	-	-	-	-	-	0.07	b.d.	b.d.	b.d.	-	-	-	b.d.	b.d.	-	-	-	-	-	-
		LP_s5-mat	15.0	15.18	3.17	0.12	4.76	0.73	2401.41	-	-	-	-	-	-	-	0.21	79.67	0.016	0.33	-	-	-	0.84	1.94	-	-	-	-	-	-
		MLS_s3-mat§	11.0	16.82	1.74	0.02	4.16	0.22	523.94	5.83	21.95	69.91	b.d.	27.29	2.92	77.14	0.10	14.46	0.003	0.24	0.01	0.11	4.59	0.15	1.39	0.16	0.38	0.72	b.d.	0.42	0.39
		EST_s2-mat§	6.8	16.63	1.74	0.01	4.76	1.40	742.25	1.76	7.41	94.95	0.57	16.73	3.51	75.49	0.10	8.15	0.004	0.05	0.03	0.21	4.54	0.09	0.31	0.05	0.13	0.99	0.25	0.82	0.38
	Sandstones	LP_s3-sed§	15.0	1.30	0.46	0.05	0.26	b.d.	b.d.	1.45	b.d.	b.d.	b.d.	0.72	0.16	4.88	0.36	413.91	b.d.	b.d.	0.12	0.22	0.27	4.36	b.d.	0.53	b.d.	b.d.	b.d.	0.87	0.31
		MLS_s1-sed§	15.0	2.47	0.68	0.09	0.50	0.02	b.d.	2.70	9.88	16.04	b.d.	1.07	0.21	9.04	0.28	356.46	b.d.	b.d.	0.09	0.20	0.11	3.75	b.d.	0.52	1.17	1.13	b.d.	0.77	0.31
		MLS_s2-sed§	15.0	1.70	0.56	0.21	0.22	0.02	b.d.	1.71	b.d.	b.d.	b.d.	1.0	0.20	6.23	0.33	1246.45	b.d.	b.d.	0.12	0.20	0.19	13.12	b.d.	0.47	b.d.	b.d.	b.d.	0.77	0.31
		MLS_s3-sed§	11.0	1.51	0.47	0.02	0.18	0.02	b.d.	1.39	8.58	14.37	b.d.	1.73	0.27	4.93	0.31	129.33	b.d.	b.d.	0.18	0.16	0.21	1.36	b.d.	0.43	1.66	1.65	b.d.	0.61	0.27
		EST_s2-sed§	6.8	0.78	0.44	0.002	0.15	0.01	305.63	0.50	8.45	10.78	0.80	0.80	0.34	2.64	0.56	21.85	0.039	3.06	0.44	0.43	0.72	0.23	17.92	0.30	3.16	2.40	7.60	1.65	0.28

FPS: flat pyritized structure; DB: domal buildup; WS: wrinkle structure; LP: linear pattern; FR: “fairy-ring” structure; MLS: mat-layer structure; EST: “elephant-skin” texture, as described by Aubineau *et al*. (2018).

*: ppm/wt.% unit; **: wt.%/wt.% unit; §: major and trace element values from Aubineau *et al*. (2020); †: average ratio for the UCC (Rudnick & Gao, 2003); -: not measured; b.d.: below detection; #: values from Ossa Ossa (2010)

TABLE S2. Iron speciation data for all samples in this study.

Formation	Lithology	Sample ID	Height m	Fe_{Py} (wt. %)	Fe_{Carb} (wt. %)	Fe_{Ox} (wt. %)	Fe_{Mag} (wt. %)	Fe_{PRS} (wt. %)	Fe_{HR}/Fe_{T}	Fe_{Py}/Fe_{HR}	Fe_{Carb}/Fe_{HR} (%)	Fe_{PRS}/Fe_{T} 0.39 (wt.%)‡
FB2b	Pyritized MRS	FPS_s5-mat	18.70	24.15	0.39	0.86	0.09	0.15	0.95	0.95	1.53	0.01
		DB_s4-mat	17.10	15.10	0.59	0.98	0.07	0.16	0.80	0.90	3.51	0.01
		FPS_s4-mat	16.30	25.17	0.33	0.64	0.07	0.29	0.90	0.96	1.26	0.01
		FPS_s3-mat	16.20	-	-	-	-	-	-	-	-	-
		DB_s3-mat	16.00	19.10	0.31	0.86	0.08	0.18	0.97	0.94	1.54	0.01
	Black shales	WS_s2-sed	19.70	-	-	-	-	-	-	-	-	-
		GFB2-R6 1	18.75	-	-	-	-	-	-	-	-	-
		FPS_s5-sed	18.70	0.05	0.43	0.51	0.07	0.73	0.64	0.05	40.56	0.44
		AFBSO-12#	18.60						0.35	0.13		
		AFBSO-11#	18.30						0.27	0.14		
		AFBSO-10#	17.90						0.33	0.04		
		GFB2-R14 1	17.80	-	-	-	-	-	-	-	-	-
		LP_s4-sed	17.75	0.18	0.24	0.97	0.06	0.57	0.29	0.12	16.46	0.11
		AFBSO-09#	17.50						0.14	0.37		
		GFB2-R18 1	17.48	-	-	-	-	-	-	-	-	-
		GFB2-R11 1	17.45	-	-	-	-	-	-	-	-	-
		GFB2-R16 1	17.20	-	-	-	-	-	-	-	-	-
		DB_s4-sed	17.10	0.83	0.26	0.45	0.06	0.09	0.81	0.52	16.19	0.05
		B01 1	17.10	-	-	-	-	-	-	-	-	-
		GFB2-R19 1	17.05	-	-	-	-	-	-	-	-	-
		GFB2-R12 1	16.85	-	-	-	-	-	-	-	-	-
		GFB2-R13 1	16.55	-	-	-	-	-	-	-	-	-
		JN35 1	16.25	-	-	-	-	-	-	-	-	-
		FPS_s3-sed	16.20	0.17	0.06	0.06	0.07	0.15	0.22	0.47	16.52	0.09
		AFBSO-06#	16.10						0.14	0.32	-	-
		DB_s2-sed	16.00	-	-	-	-	-	-	-	-	-
		FR_s1sed	16.00	0.33	0.33	0.37	0.06	0.06	0.66	0.30	30.06	0.04
		GFB2-R4 1	15.65	-	-	-	-	-	-	-	-	-
		MLS_s9-sed	15.50	-	-	-	-	-	-	-	-	-
		AFBSO-05#	15.30						0.14	0.51		
FB2a	Pyrite-poor MRS	MLS_s1-mat	15.0	-	-	-	-	-	-	-	-	-
		MLS_s2-mat	15.0	1.89	0.29	1.35	0.06	0.00	0.54	0.53	8.20	0.00
		EST_s3-mat	15.0	0.05	0.37	0.58	0.06	0.10	0.44	0.05	34.90	0.04
		MLS_s6-mat	15.0	-	-	-	-	-	-	-	-	-
		MLS_s4-mat	15.0	0.16	0.05	1.15	0.07	0.27	0.36	0.11	3.57	0.07
		MLS_s5-mat	15.0	0.20	0.35	1.62	0.07	0.20	0.50	0.09	15.69	0.04
		MLS_s10-mat	15.0	0.00	0.28	0.43	0.08	0.05	0.91	0.00	35.64	0.06
		LP_s5-mat	15.0	0.12	0.05	0.78	0.06	0.32	0.32	0.12	4.61	0.10
		MLS_s3-mat	11.0	0.43	0.05	0.05	0.07	0.07	0.34	0.72	7.77	0.04
		EST_s2-mat	6.8	0.00	0.06	0.00	0.07	0.07	0.07	0.00	45.20	0.04

Sandstones	LP_s3-sed	15.0	-	-	-	-	-	-	-	-	-
	MLS_s1-sed	15.0	-	-	-	-	-	-	-	-	-
	MLS_s2-sed	15.0	-	-	-	-	-	-	-	-	-
	MLS_s3-sed	11.0	-	-	-	-	-	-	-	-	-
	EST_s2-sed	6.8	-	-	-	-	-	-	-	-	-

FPS: flat pyritized structure; DB: domal buildup; WS: wrinkle structure; LP: linear pattern; FR: “fairy-ring” structure; MLS: mat-layer structure; EST: “elephant-skin” texture, as described by Aubineau *et al*. (2018).

‡: average Paleozoic shale value (Raiswell *et al*., 2008); -: not measured; #: values from Ossa Ossa (2010).

TABLE S3. Carbon and nitrogen data.

Formation	Lithology	Sample ID	Height m	$\delta^{13}C_{org}$ (‰, V-PDB)	TOC (wt. %)	$\delta^{15}N_{WR}$ (‰, Air)	TN (wt. %)	$\delta^{15}N_{kerogen}$ (‰, Air)
FB2b	Pyritized MRS	FPS_s5-mat	18.7	-33.4	0.56	-2.0	0.06	-
		LP_s4-mat	17.8	-33.4	0.87	-2.5	0.10	-
		DB_s4-mat	17.1	-34.4	-	-0.2	0.07	-
		FPS_s4-mat	16.3	-33.2	0.23	b.d.	*0.04*	-
		FPS_s3-mat	16.2	-34.6	0.87	b.d.	*0.04*	-
		DB&FPS_s1-mat	16.2	-33.8	0.60	0.3	0.05	-
		DB_s3-mat	16.0	-33.2	0.50	-3.3	0.06	-
	Black shales	WS_s2-sed	19.7	-33.2	0.63	-0.3	0.08	-
		FPS_s5-sed	18.7	-35.3	3.67	-0.6	0.07	2.3
		LP_s4-sed	17.8	-36.2	0.67	b.d.	*0.05*	-
		DB_s4-sed	17.1	-35.2	2.81	-0.5	0.08	1.5
		FPS_s3-sed	16.2	-35.2	3.25	-0.1	0.06	-0.2
		DB_s2-sed	16.0	-35.4	3.02	0.1	0.08	1.9
		FR_s1-sed	16.0	-34.9	1.73	0.6	0.08	1.6
		FR_s2-sed	16.0	-35.5	2.35	0.3	0.07	-
		MLS_s9-sed	15.5	-34.7	1.75	-0.8	0.08	-
FB2a	Pyrite-poor MRS	MLS_s1-mat	15.0	-34.5	4.85	0.2	0.12	-
		MLS_s2-mat	15.0	-33.7	8.13	0.7	0.15	-
		EST_s3-mat	15.0	-30.1	12.71	0.3	0.11	2.4
		MLS_s6-mat	15.0	-34.0	4.59	0.6	0.13	0.9
		MLS_s4-mat	15.0	-34.0	8.55	0.7	0.12	2.1
		MLS_s5-mat	15.0	-35.2	8.93	0.8	0.13	-
		WS_s3-mat	15.0	-34.1	4.32	1.4	0.14	-
		MLS_s10-mat	15.0	-32.2	18.24	1.8	0.16	3.6
		LP_s5-mat	15.0	-34.2	2.55	-0.1	0.14	2.3
		EST_s5-mat	15.0	-30.8	8.85	-0.3	0.10	-
		MLS_s3-mat	11.0	-33.2	1.45	1.4	0.10	-
		EST_s2-mat	6.8	-30.7	7.79	-3.5	0.13	-
	Sandstones	LP_s3-sed	15.0	-33.5	0.19	b.d.	*0.01*	-
		MLS_s10-sed	15.0	-31.7	0.34	b.d.	*0.01*	-
		MLS_s1-sed	15.0	-32.4	0.16	b.d.	*0.01*	-
		MLS_s2-sed	15.0	-30.8	0.29	b.d.	*0.01*	-
		MLS_s3-sed	11.0	-30.5	0.39	b.d.	*0.01*	-
		EST_s2-sed	6.8	-30.1	0.33	b.d.	*0.01*	-

FPS: flat pyritized structure; LP: linear pattern; DB: domal buildup; WS: wrinkle structure; FR: “fairy-ring” structure; MLS: mat-layer structure; EST: “elephant-skin” texture, as described by Aubineau *et al.* (2018).

-: not measured; b.d.: below detection. Italicized values: samples where data are close to the detection limit.